



Self-healing performance and corrosion resistance of a bilayer calcium carbonate coating on microarc-oxidized magnesium alloy

Ye Wang^a, Di Yu^a, Kai Ma^a, Chaoneng Dai^a, Danqian Wang^{a,*}, Jingfeng Wang^{a,b,*}

^a College of Materials Science and Engineering, Chongqing University, Chongqing 400045, China

^b National Engineering Research Center for Magnesium Alloys, Chongqing University, Chongqing 400044, China

ARTICLE INFO

Keywords:

Magnesium alloy formwork
Calcium carbonate
Ultrasound-assisted chemical conversion
Corrosion
Surface

ABSTRACT

A CaCO₃ coating with good anticorrosion and self-healing performance was fabricated on the as-prepared MAO coating on the surface of AZ41 Mg alloy via ultrasound-assisted chemical conversion, a DCPD(CaHPO₄·H₂O) coating was also fabricated on the MAO coating as a comparison. Surface characterizations were carried out to obtain the morphology and composition of CaCO₃ coating formed and electrochemical methods were adopted to assess the corrosion resistance of Mg alloy embedded in PC paste. The self-healing property of MAO/CaCO₃ coating was ascribed to the formation of extra calcite. This coating may become a potential target for surface modification of magnesium alloy formwork.

1. Introduction

Concrete is one of the most important building materials in civil engineering and fresh poured concrete is usually supported and shaped by the concrete formwork [1]. Conventional steel and wood concrete formwork are gradually replaced by the aluminum formwork due to the disadvantage of overweight and lack of efficient mechanical property [2]. However, it is increasingly claimed that the surface of aluminum alloy formwork becomes inhomogeneous after the removal of cured concrete because of the reaction of aluminum alloy in highly alkaline concrete [3]. Recently, magnesium alloy formwork is emerging due to its more light-weighted feature, which is only two-thirds of the density compared to aluminum [3]. In addition, different from aluminum alloy, the magnesium alloy has been proved to be stable in alkaline conditions due to the formation of insoluble Mg(OH)₂ on the surface of Mg alloys [4]. However, presence of chloride ions in concrete reduces the corrosion resistance of magnesium alloys and hampers the applications of magnesium alloy products.

Surface treatment is considered as one of the best methods for corrosion protection of magnesium alloy [5–14]. Among the preparation for protective coatings, micro-arc oxidation (MAO) is one of the most promising methods for magnesium alloy formwork due to its excellent adhesion to the substrate as well as the high corrosion resistance [15]. However, pores and micro-cracks caused by the thermal stresses at the sites of the discharge channels and the gas evolution through the molten

oxide during the MAO process usually become transportation channels and increase the opportunity for penetration of the aggressive media [16]. Thus, a post-sealing process is required to improve the corrosion protection of the MAO coatings.

In previous researches, calcium phosphorus (Ca/P) coatings have been widely used to seal the micro-arc oxide coatings [17,18]. For instance, Kim et al. [19] developed a two-step surface treatment to restrain the rapid primary degradation of a biodegradable Mg alloy. The MAO coating was firstly performed in alkaline electrolytes and then the Ca-EDTA solution was used to fabricate the upper Ca/P coating via hydrothermal treatment. However, the improvement of corrosion resistance of calcium phosphorus coatings prepared by chemical conversion method is not very significant, and even decreases in some cases. For example, Wu et al. [18] fabricated a MAO/Ca/P coating on AZ31 Mg, although the corrosion potential enhanced compared to the neat MAO coating, but the current density decreased by one magnitude, indicating no obvious increase in the corrosion resistance. Furthermore, the corrosion behavior of Ca/P sealed MAO coatings in concrete systems has not been studied. Besides traditional calcium phosphate coatings, the CaCO₃ coating has been investigated recently [20]. Compared to calcium phosphate, CaCO₃ is more stable in alkaline conditions and can be used for large scale. Different from early researches which focus on the preparation of CaCO₃ coatings with CaCO₃ suspensions [21], resulting in the limited enhancement on the corrosion resistance because of the lack of enough density, one kind of CaCO₃ coating has been investigated

* Corresponding authors at: College of Materials Science and Engineering, Chongqing University, Chongqing 400045, China.

E-mail addresses: wang.danqian@cqu.edu.cn (D. Wang), jingfengwang@163.com (J. Wang).

recently by the chemical conversion method with continuous layered structure and the corrosion resistance can thus be improved [20]. Therefore, it is plausible that the calcium carbonate could seal the pores on the micro-arc oxide coatings and enhance the corrosion resistance of the MAO coatings.

In this work, the MAO coating was produced in the phosphate-containing electrolyte. Afterwards, both $\text{CaHPO}_4 \cdot \text{H}_2\text{O}$ (DCPD) and CaCO_3 coatings were fabricated on the surface of MAO coatings to seal the pores. Ultrasonic was applied to assist the formation of the DCPD and CaCO_3 coatings. According to the previous literature [22], the denser coating could be obtained via the ultrasonic-assisted treatment due to the cavitation effect, which has significantly influence on the nucleation and growth of crystals. The synthesis process is exhibited in Fig. 1. Afterwards, the composition and morphologies of the MAO, MAO/DCPD and MAO/ CaCO_3 coatings were characterized and the corrosion resistance of the coatings was also investigated in the chloride-containing Portland cement system up to 96 h. Finally, both the formation and corrosion protection mechanism were proposed and discussed.

2. Materials and methods

2.1. Materials

The mean composition of AZ41 Mg alloy is Al 4.3 wt %, Mn 0.4 wt %, Zn 0.9 wt % and balance Mg. Sodium hydroxide (NaOH, 99 %), Sodium phosphate (Na_3PO_4 , 99 %), Sodium bicarbonate (NaHCO_3 , 99 %) were purchased from Chongqing Chuandong Chemical Reagent Co. Ltd., China. Sodium dihydrogen phosphate (NaH_2PO_4 , 99 %) and Calcium nitrate ($\text{CaN}_2\text{O}_6 \cdot 4\text{H}_2\text{O}$, 99 %) were purchased from Chengdu Kelong Chemical Reagent Co. Ltd., China.

2.2. Fabricating of MAO coating

As-cast AZ41 magnesium alloys were cut into $10 \text{ cm} \times 10 \text{ cm} \times 3 \text{ cm}$ pieces for this investigation. The samples mechanically ground to #1500 with SiC paper, then, they were rinsed with ethanol at ambient temperature and rapidly dried with hot air. Then, the hybrid (5 g/L NaOH and 5 g/L Na_3PO_4) bath solution was placed in the reaction tank for continuous stirring, always maintained at $25 \pm 5 \text{ }^\circ\text{C}$ through the condensation circulation system. Then, the bare AZ41 substrate was placed in the hybrid bath solution. A square electrical signal pulse AC power supply (Hipims, China) was used to perform work on the AZ41 Mg alloy for 300 s. The pulse width is 100 μs with the frequency of 500 Hz. The AZ41 specimen with the MAO coating was rinsed with ultrasonic and ethanol, and dried with hot air for use. The resulting sample was designated as MAO coating.

2.3. Fabricating of MAO/DCPD and MAO/ CaCO_3 coatings

A conventional ultrasonic cleaner was used for chemical conversion and producing ultrasound. Beakers with a mixture 30 mL of 0.5 M NaHCO_3 and 90 mL of 0.5 M $\text{CaN}_2\text{O}_6 \cdot 4\text{H}_2\text{O}$ was prepared to fabricate CaCO_3 coating, a mixture 30 mL of 0.5 M NaH_2PO_4 and 90 mL of 0.5 M $\text{CaN}_2\text{O}_6 \cdot 4\text{H}_2\text{O}$ was prepared to fabricate DCPD coating. The ultrasound-assisted chemical conversion was conducted at a frequency of 40 kHz for 15 min $60 \text{ }^\circ\text{C}$ in the ultrasonic cleaner. These two coatings were named MAO/DCPD coating and MAO/ CaCO_3 coating, respectively. After the treatments, the samples were taken out, washed with deionized water and ethanol in turns and then dried with hot air.

2.4. Characterization and test

Field emission scanning electron microscope (FESEM, FEI Nova400) was used to observe the surface and cross-section morphologies of the treated samples and the elemental distribution of the treated samples were analyzed by energy dispersive X-ray spectrometer (EDS).

Grazing incidence X-ray diffraction analyses (GIXRD, Rigaku D/Max 2500PC) were performed to characterize the surface phase composition of the investigated samples with $\text{Cu K}\alpha$ radiation and X-ray incidence $\alpha = 2^\circ$ was selected in this investigation. The step side employed in this study was 0.02° in the 2θ range from 10° to 80° .

X-ray photoelectron spectroscopy (XPS, PHI-5000 Versa Probe III, ULVAC-PHI, Japan) was employed to examine the composition of the coatings formed on the AZ41 alloy. The K-Alpha XPS system was used which is high throughput monochromated and capable of highly automated data acquisition. The high-resolution spectra of O1s, C1s, P 2p and Mg1s were measured.

2.5. Corrosion evaluation

Electrochemical tests were conducted on a Gamry Interface 1011E Potentiostat with Gamry Framework software, and the three-electrode technique was used, which equips with a saturated calomel electrode (SCE) as reference electrode and a stainless-steel bar as counter electrode, the investigated samples as working electrode. The working electrode was embedded in a PC paste mixed with 3.5 wt % NaCl with the dimension of $20 \text{ mm} \times 20 \text{ mm} \times 20 \text{ mm}$, each time before electrochemical tests, the PC paste specimens were submerged in water for 20 min to ensure the conductivity. Firstly, electrochemical impedance spectra (EIS) were collected in a frequency range from 100KHZ to 10mHZ with a sinusoidal AC perturbation with an amplitude of 5 mV. Prior to the EIS measurement, the sample is stabilized in the solution for 10 min until the corrosion potential reached a steady state. Subsequently, potentiodynamic polarization curves were recorded with a scan

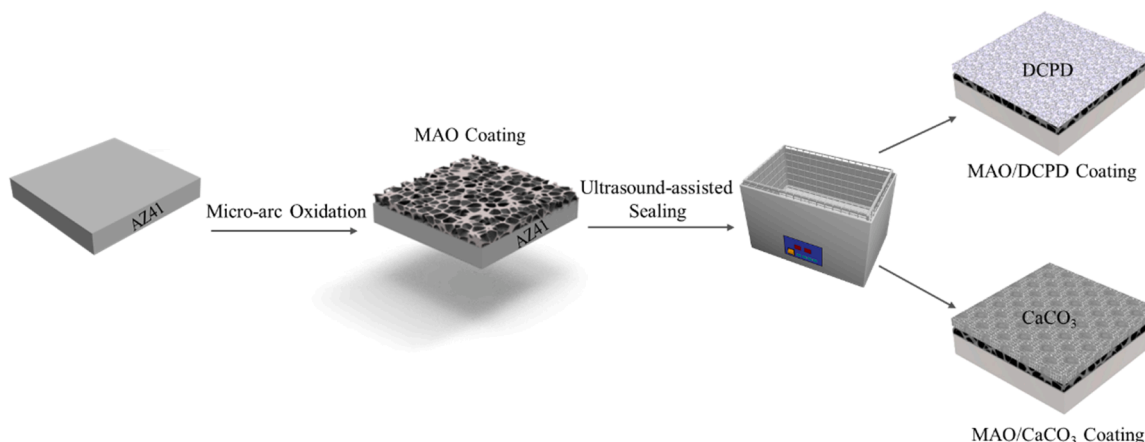


Fig. 1. : Schematic diagram of the ultrasound-assisted synthesis process of MAO/DCPD and MAO/ CaCO_3 coatings on AZ41 magnesium alloy.

range from $-0.9 V_{ocp}$ to $0.9 V_{ocp}$ at a scan rate of 1 mV/s. The EIS data were fitted by ZSimpWin software. After embedded in PC paste for 96 h, prior to the surface analysis, the samples were taken out and rinsed with deionized water and ethanol in turns and then dried with hot air.

Solution immersion test was conducted in the simulated concrete solution (0.1 mol/L NaOH + 0.2 mol/L KOH + 0.1 mol/L $Ca(OH)_2$ + 0.003 mol/L $CaSO_4$) with 3.5 wt % NaCl. The MAO, MAO/DCPD and MAO/ $CaCO_3$ coatings were immersed in the solution for 96 h and then taken out, washed with deionized water. SEM observation was conducted to reveal the surface morphology.

3. Results and discussion

3.1. Morphology and composition of the coatings on AZ41 alloy

3.1.1. Surface morphology

The surface morphologies of the as-prepared coatings on the surface of AZ41 alloy are presented in Fig. 2. As shown in Fig. 2(a), the surface of the MAO coating is smooth. However, the enlarged image in Fig. 2(d) shows that the MAO coating is composed of pores and micro-cracks, which is a typical feature of MAO coating caused by the thermal stresses at the sites of the discharge channels and the gas evolution through the molten oxide during the MAO process [23]. As a comparison, the original pores and micro-cracks all disappeared on the surface of both MAO/DCPD and MAO/ $CaCO_3$ coatings as shown in Fig. 2(b) and (c). This demonstrates that both DCPD and $CaCO_3$ particles formed via the ultrasonic-assisted treatment seal the pores in MAO coating well and cover the entire surface, which could be associate with the auxiliary effect of ultrasonic cavitation [24]. Moreover, comparing the morphologies of MAO/DCPD and MAO/ $CaCO_3$ coatings, it can be found that the shape and size of these coatings are significantly different. For the MAO/DCPD coating, the particles are irregularly flake-shaped with an average diameter of c.a. 5 μm . In contrast, the MAO/ $CaCO_3$ coating has a hierarchically well-ordered structure, which mainly consists of closely packed particles. Moreover, the average diameter of the particles in the MAO/ $CaCO_3$ coating is less than 5 μm , which is smaller than those in

MAO/DCPD coating. Furthermore, it can be observed that the MAO/ $CaCO_3$ coating is composed of both cubic particles and spherical particles, which could indicate that the MAO/ $CaCO_3$ coating is possibly composed of different types of $CaCO_3$.

3.1.2. Surface composition

In order to confirm the chemical composition of the MAO, MAO/DCPD, MAO/ $CaCO_3$ coatings fabricated on the surface of AZ41 alloy, XPS analysis was first performed to obtain the information on the outermost regions of the coatings and the results are shown in Fig. 3. It can be seen from the XPS full survey spectra of the coatings in Fig. 3(a) that the Mg and O peaks appear in the spectrum of the MAO coating, which could mainly originate from the MgO layer. On the contrary, the signal of Mg1s is absent while Ca and P elements appeared in the spectrum of the MAO/DCPD coating, indicating that the surface of the MAO coating has been fully covered with the Ca/P layer after the ultrasound-assisted conversion treatment. As a comparison, both Ca and O elements can be detected in the spectra of the MAO/ $CaCO_3$ coating. This demonstrates that the outermost of MAO/ $CaCO_3$ coating possibly mainly consists of $CaCO_3$. Moreover, it can be observed the signal of Mg 1 s also appear in the spectra of the MAO/ $CaCO_3$ coating, the intensity of which is even higher than that of the MAO coating.

In order to further investigate the composition of the MAO, MAO/DCPD, MAO/ $CaCO_3$ coatings, the deconvolution of the O 1 s, C 1 s and P 2p high resolution XPS spectra were carried out as shown in Fig. 3(b)–(e). The O 1 s spectra of all the coatings mainly have the peak around 530.8 eV, which can be assigned to MgO [25]. Moreover, peaks at 532.2 eV and 533.5 eV appear in the O 1 s XPS spectrum of MAO/DCPD coating, which can be ascribed to the $CaHPO_4$ [26]. This confirms the formation of Ca/P coating on the surface of the MAO coating. Moreover, a weak peak at 532.8 eV corresponding the bound H_2O also appear in the O 1 s XPS spectrum of MAO/DCPD coating [27]. As a comparison, the O 1 s spectrum of the MAO/ $CaCO_3$ coating can be deconvoluted into three peaks. In addition to the peak of MgO at 530.8 eV, the peak at 531.7 eV corresponding to $CaCO_3$ also exists in the O 1 s spectrum of the MAO/ $CaCO_3$ coating [28]. Moreover, it is worthwhile to note that a

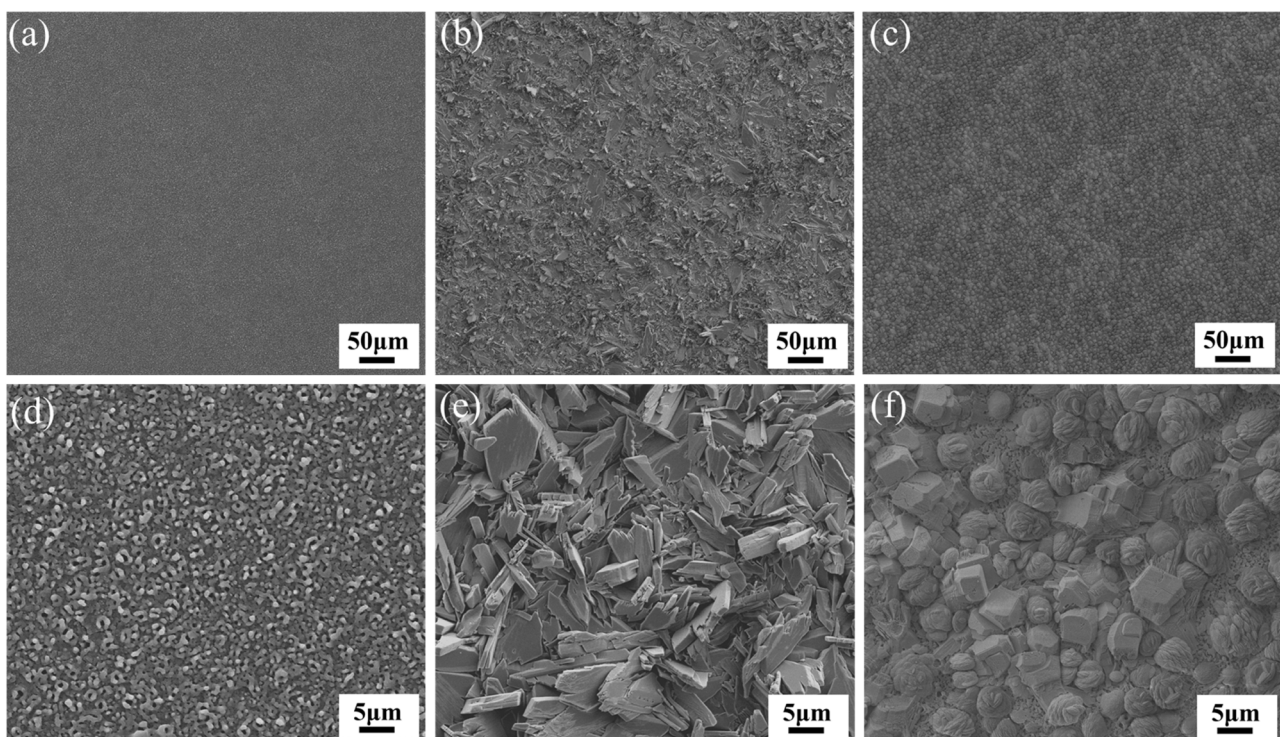


Fig. 2. : Surface morphologies of (a, d) MAO coating, (b, e) MAO/ DCPD coating and (c, f) MAO/ $CaCO_3$ coating.

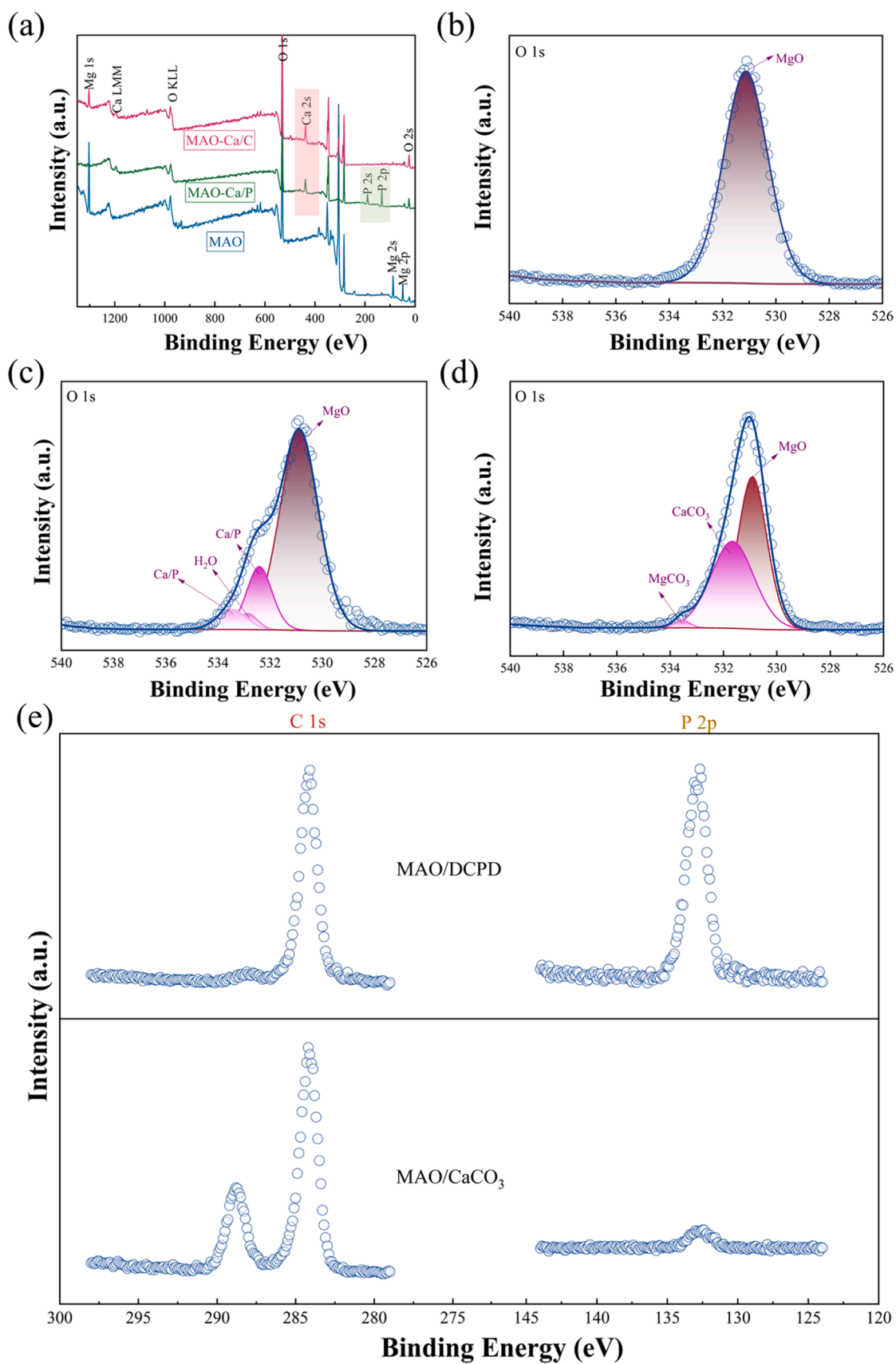


Fig. 3. : XPS analysis of the treated samples. (a) Broad survey, high-resolution survey of O 1s survey of (b) MAO coating, (c) MAO/DCPD coating and (d) MAO/CaCO₃ coating, (e) C 1s survey and P 2p survey of MAO/DCPD coating and MAO/CaCO₃ coating.

weak peak at 533.4 eV also appears in the O 1 s spectrum of the MAO/CaCO₃ coating, which can be ascribed to MgCO₃ [29]. This indicates that slight contents of MgCO₃ was incorporated into the CaCO₃ layer. Additionally, Fig. 3(e) presents the comparison of C 1 s and P 2p spectra between the MAO/DCPD and MAO/CaCO₃ coatings. It can be observed that the deconvoluted C 1 s peaks of both MAO/DCPD and MAO/CaCO₃ coatings exhibit peak at 284.8 eV, which can be ascribed to C-C/C-H possibly originating from the contamination of the surface during the specimen preparation [30]. In addition, the C 1 s peak of MAO/CaCO₃ coating exhibits a peak at 289.1 eV corresponding to CO₃²⁻ [31], also confirms the formation of CaCO₃ coating on the surface of the MAO/CaCO₃ coating. Additionally, P 2p peak is absent in the XPS spectrum of the MAO/CaCO₃ coating. As a comparison, the deconvoluted P 2p peak of the MAO/DCPD coating only exhibit a peak at 132.6 eV assigned to HPO₄²⁻ [32], which is indicative of the formation of Ca/P layer of MAO/DCPD coating.

The component phases of the coatings formed on the surface of AZ41 alloy via micro-arc oxidation and subsequent ultrasound-assisted treatment were further analyzed via GIXRD at an incident angle of 2°. The resultant GIXRD patterns of the coatings as well as the standard MgO, CaCO₃(calcite, vaterite), MgCO₃, CaHPO₄·2H₂O (DCPD) and metallic Mg are shown in Fig. 4. It can be seen that MgO peaks were obtained from the MAO, MAO/DCPD and MAO/CaCO₃ coatings, which originates from the MAO layer. Moreover, the signal of the metallic Mg can also be obtained in all the MAO, MAO/DCPD and MAO/CaCO₃ coatings, which could originate from the AZ41 substrate through the pores in the MAO layer. Nevertheless, the intensities of the Mg peaks of the MAO/DCPD and MAO/CaCO₃ coatings are lower than those of the MAO coating, which demonstrates that the pores in the MAO layer were mostly sealed via the ultrasound-assisted conversion treatments. Furthermore, the MAO/DCPD coating produces the characteristic peaks of CaHPO₄·2H₂O (DCPD), indicating the DCPD particles have been attached to the surface of the MAO coating after the sealing treatment by the assistance of ultrasound. In addition, several peaks of Mg(OH)₂ with low intensities can also be seen from the GIXRD spectrum of the MAO/DCPD coating, indicating that a thin layer of Mg(OH)₂ was possibly formed beneath the DCPD layer. Similar observation has also been found in the previous study which showed that the peaks of Mg(OH)₂ exist in the XRD pattern of the calcium phosphate coating on micro-arc oxidized magnesium by chemical deposition [33]. The presence of Mg(OH)₂ layer beneath the DCPD layer could be related to the dissolution of the MgO layer, which will be further discussed in Section 3.3.1. On the other hand, typical

peaks of calcite and vaterite are collected in the GIXRD pattern for the MAO/CaCO₃ coating, which were usually of cubic and spherical respectively as demonstrated in the previous studies [34]. This is well corroborated with the SEM observations in Fig. 2(c). In addition, the presence of MgCO₃ in the GIXRD pattern for the could imply that MgCO₃ probably forms in the CaCO₃ layer of the MAO/CaCO₃ coating. The detailed discussion on the mechanism of the coating growth will be mentioned in Section 3.3.1.

3.1.3. Cross-section morphology and composition

In order to further identify the structure of the MAO, MAO/DCPD and MAO/CaCO₃ coatings, the cross-sectional morphologies and corresponding EDS analysis were obtained via SEM observation and the results are presented in Fig. 5. It can be observed from Fig. 5(a) that the thickness of the as-prepared MAO coating is c.a. 2 μm. The post sealing process via the ultrasound-assisted Ca/P chemical conversion treatment leads to the formation of a much thicker MAO/DCPD coating (c.a. 6.3 μm) compared to the MAO coating. As a comparison, the thickness of the MAO/CaCO₃ coating (c.a. 2.5 μm) is only slightly higher than that of the MAO coating. Moreover, the MAO/CaCO₃ coating is much smoother than the MAO/DCPD coating, which could contribute to the integrity and the anticorrosive property of the coating. Furthermore, it can be noted that both the DCPD and CaCO₃ layers adhere well to the MAO layer, which could be beneficial from the assistance of ultrasonic treatment. The EDS analysis provides more detailed information on the composition distributions of the MAO, MAO/DCPD and MAO/CaCO₃ coatings. It can be seen from Fig. 5(b) that only Mg and O elements exist in the MAO coating, indicating that the MAO coating mainly consists of MgO, which is consistent with the GIXRD results in Fig. 4. As a comparison, the EDS results of the MAO/DCPD coating in Fig. 5(d) show that the MAO/DCPD coating has a dual-layered structure, which consists an inner MgO layer and an outer Ca/P layer. This indicates that a layer of DCPD was covered on the surface of the MAO layer. Moreover, it can be noted that the thickness of the inner layer of the MAO/DCPD coating is similar to that of the MAO coating, which indicates that the Ca/P layer mainly formed on the surface of the MAO layer. Furthermore, it is noted that, unlike the traditional Ca/P coatings prepared on the magnesium substrate by chemical conversion, no cracks were found from the cross-sectional morphology. This could benefit from the MAO layer which reduces the dissolution of magnesium substrate and thus the hydrogen evolution is suppressed. As a comparison, a triple-layer structure can be observed from the EDS analysis in Fig. 5(f). In addition to the inner MgO layer and the outer CaCO₃ layer, a middle layer containing Mg, Ca, O, C can be observed between the two layers. This indicates that a thinner (Mg,Ca)CO₃ layer formed beneath the outer CaCO₃ coating, which is in consistence with the GIXRD results. Moreover, it can be seen that the MgO layer in the MAO/CaCO₃ coating is thinner than that in MAO and MAO/DCPD coatings. Based on this, it could be deduced that although the dissolution process of Mg is inhibited by existence the MAO layer, the MgO in the MAO layer could still react with the Ca²⁺ and CO₃²⁻ ions in the chemical solution to form the dense (Mg,Ca)CO₃ layer, which will be further discussed in Section 3.3.1.

3.2. Anti-corrosion behavior

3.2.1. Potentiodynamic polarization curves

The anticorrosion performances of the MAO coating, MAO/DCPD coating and MAO/CaCO₃ coating embedded in the PC paste with 3.5 wt % NaCl for 96 h were analyzed via potentiodynamic polarization measurements and the resultant curves are shown in Fig. 6. Detailed electrochemical information on the corrosion kinetics and thermodynamics, including corrosion potential (E_{corr}) and corrosion current density (i_{corr}), can be obtained from Fig. 6 and the results are listed in Table 1.

It can be found from the table that, compared to the i_{corr} value of the MAO coating ($3.933 \times 10^{-6} \text{ A}\cdot\text{cm}^{-2}$), the i_{corr} value of the MAO/DCPD coating is slightly increased to $5.767 \times 10^{-6} \text{ A}\cdot\text{cm}^{-2}$, while the i_{corr}

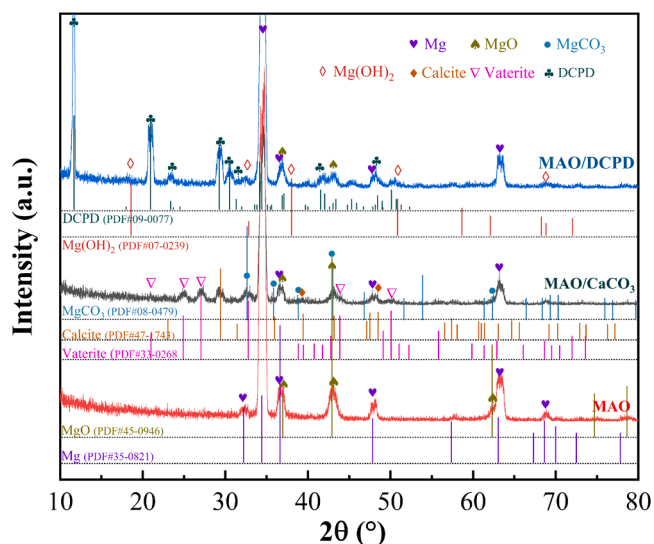


Fig. 4. : GIXRD patterns of the MAO coating, MAO/DCPD coating and MAO/CaCO₃ coating at an incident angle of 2°.

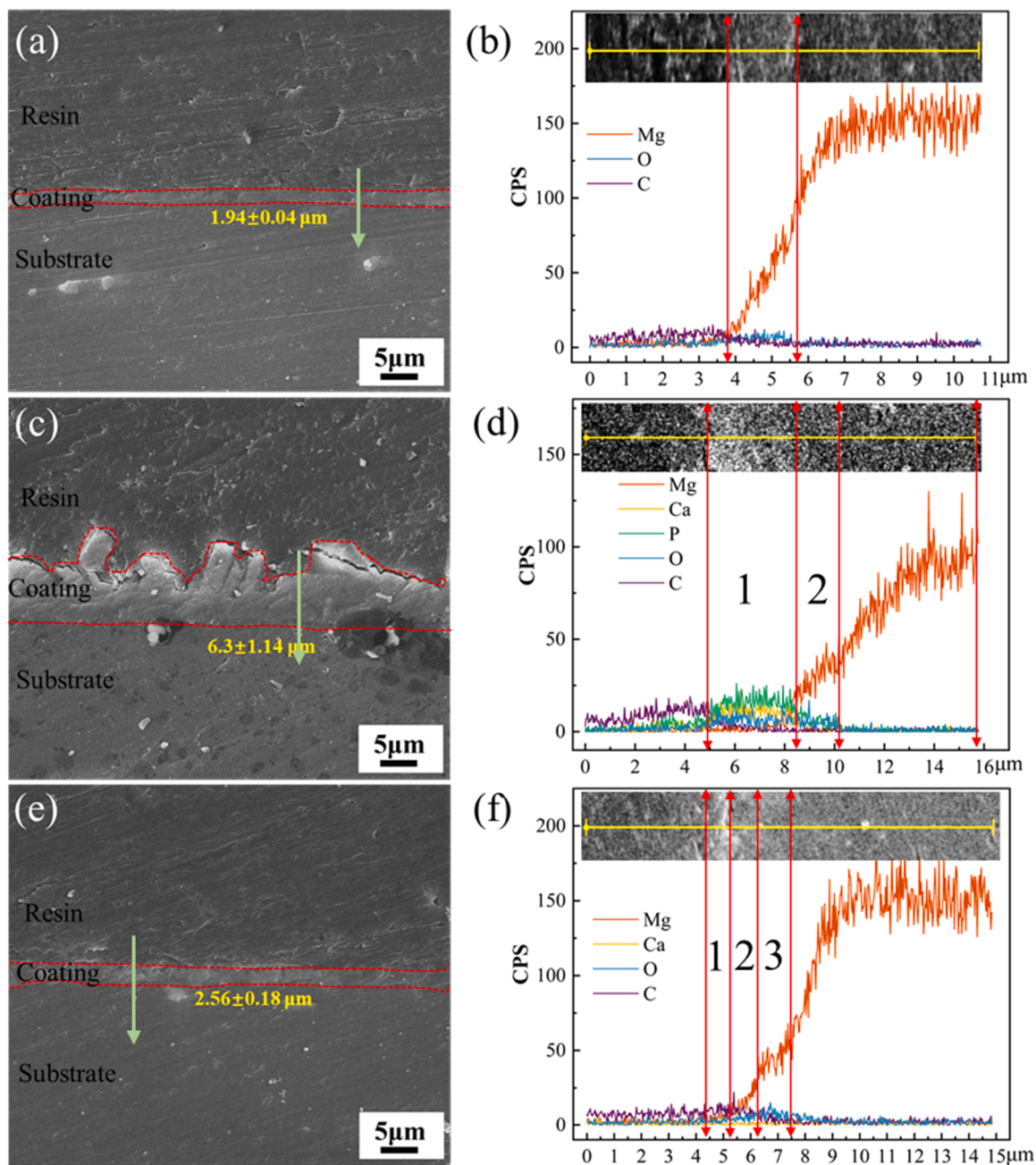


Fig. 5. : Cross-sectional morphologies of (a) MAO coating, (c) MAO/DCPD coating, (e) MAO/ CaCO_3 coating and corresponding EDS analysis of (b) MAO coating, (d) MAO/DCPD coating (f) MAO/ CaCO_3 coating.

value of the MAO/ CaCO_3 coating ($3.229 \times 10^{-7} \text{ A}\cdot\text{cm}^{-2}$) is more than one order of magnitude lower than that of the MAO coating. This demonstrates that although the DCPD layer is thicker than CaCO_3 layer, the MAO/ CaCO_3 coating shows better corrosion resistance than the MAO/DCPD coating. This could be benefitted by the compact inner (Mg, Ca) CO_3 layer resulting from the ultrasonic treatment as mentioned before. The detailed discussion will be elaborated in Section 3.3.2. In addition, the E_{corr} of the MAO/ CaCO_3 coating (-0.154 V) becomes much more positive than that of the MAO coating (-0.488 V), suggesting that the protective capability of the MAO/ CaCO_3 coating much improves compared to that of the MAO coating. On the contrary, the E_{corr} of the MAO/DCPD coating (-0.540 V) is more negative than that of the MAO coating, which could demonstrate that the corrosion resistance of the MAO/DCPD coating is less than that of the MAO coating. Furthermore, it can be observed that the E_{corr} values of all the coatings

are significantly ennobled compared to the corrosion potential of the bare magnesium (-1.44 V), which results in the transformation of the dominant cathodic corrosion reaction from the hydrogen reduction reaction to the oxygen reduction reaction.

3.2.2. Surface morphology and composition after corrosion

The surface morphologies of the MAO, MAO/DCPD, MAO/ CaCO_3 coatings after embedded in PC paste with 3.5 wt % NaCl for 96 h were characterized as shown in Fig. 7. It can be observed that the MAO/ CaCO_3 coating after immersion shows a completely different surface feature compared to those of the MAO and MAO/DCPD coatings. It can be observed from Fig. 7(a), (b), (d) and (e) that porous corrosion products formed on the surface of both the MAO and MAO/DCPD coatings. Furthermore, the $\text{CaHPO}_4 \cdot 2\text{H}_2\text{O}$ particles fall off in some areas in the MAO/DCPD coating and the remaining particles also no longer

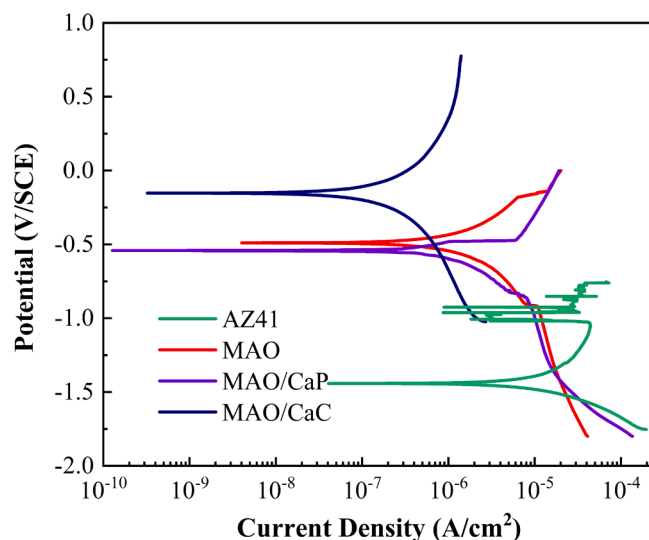


Fig. 6. : Potentiodynamic polarization curves of samples embedded in PC paste with 3.5 wt %NaCl for 96 h.

Table 1

Corrosion potential and corrosion current density determined from polarization curves.

	E_{corr} (V/SCE)	I_{corr} ($A \cdot cm^{-2}$)
AZ41	-1.44	3.221×10^{-5}
MAO	-0.488	3.933×10^{-6}
MAO/CaP	-0.540	5.767×10^{-6}
MAO/CaC	-0.154	3.229×10^{-7}

retain their original intact morphology. This indicates that severe corrosion occurs on the MAO and MAO/ DCPD specimens, which is well corroborated with the potentiodynamic polarization results as shown in Fig. 6. Fig. 7(a1–a4) present the results of the EDS analysis which reveals that the MAO coating after embedment mainly consists of Mg, O, Si elements. The Mg and O elements mainly come from the coating while the Si element stems from PC paste. Fig. 7(b1–b5) show the results of the EDS analysis of the MAO/DCPD coating after embedment. It indicates that part of the DCPD coating was damaged, the Ca and P elements were replaced by the Mg and O elements. Then, the Si element can also be observed. On the contrary, it can be observed from the surface morphology in Fig. 7(e) that the MAO/ CaCO₃ coating remains relatively stable, which is significantly more compact than the corresponding MAO/ DCPD coating. This suggests that the MAO/ CaCO₃ coating can efficiently improve the protective capability in PC paste. Furthermore, the enlarged morphology of the MAO/ CaCO₃ coating in Fig. 7(f) shows that, whilst some PC pastes are covered on the surface, the particles beneath the pastes keep intact. The EDS analysis in Fig. 7(c1–c5) also demonstrates that the MAO/ CaCO₃ coating mainly consists of the Ca, O and C elements, the Si element from PC paste can also be observed. Considering both corrosion resistance and the demolding of concrete cured in the magnesium alloy formwork, the design of super-hydrophobic surface is needed for the magnesium alloy formwork, which will be further investigated in our future study. In order to observe the morphology of the coatings after corrosion more clearly, the surface morphology of the coatings after being immersed in the PC pore solution for 96 h were also observed as will be mentioned below.

The chemical compositions of the three coatings after being embedded in PC paste with 3.5 wt % NaCl for 96 h was characterized by GIXRD test at an incident angle of 2°. The obtained XRD patterns of the samples as well as the standard MgO, MgCO₃, Mg(OH)₂, CaCO₃(calcite), Mg₂CO₃(OH)₂·3H₂O and metallic Mg are shown in Fig. 8.

It can be observed from the XRD patterns that the MAO coating after

embedment mainly consists of Mg, MgO and Mg(OH)₂. The MgO and Mg(OH)₂ could be related to the formation of the MAO coating and the corrosion products formed in the MAO coating as shown in Fig. 7, respectively [35]. Furthermore, one peak of Mg₂CO₃(OH)₂·3H₂O appears in the pattern, which could be generated from the interaction between the Mg(OH)₂ and pore solutions in PC paste. Moreover, for the XRD pattern of the MAO/ DCPD coating, the XRD peaks corresponding to Mg, MgO and DCPD exist, which originates from the MAO and DCPD layers of the coating. In addition, the XRD peaks assigned to Mg(OH)₂ were also obtained. This indicates that the corrosion products formed in the MAO/ DCPD coating, which is consistent with the SEM observation in Fig. 7. As a comparison, no peaks of Mg(OH)₂ can be seen from the pattern of the MAO/ CaCO₃ coating, indicating no obvious corrosion occurred during the embedment. Furthermore, in addition to the original peaks of vaterite and calcite, more peaks of calcite can be observed in the GIXRD pattern of the MAO/ CaCO₃ coating after immersion. As it is known that the calcite is more stable than vaterite [36], it could be deduced that the regrowth of CaCO₃ coating may occur during the embedment in the PC paste, which is possibly responsible for the self-healing property.

3.2.3. Long-term electrochemical measurements

Electrochemical impedance spectroscopy is often employed to evaluate the protective property of coatings. Fig. 9 presents the evolution of EIS spectra for the coated specimens including Bode plots and Nyquist plots over embedment time in PC paste with 3.5 wt %NaCl. It can be found from Fig. 9(a) that the Bode impedance values at the low frequency of the MAO, MAO/ DCPD and MAO/ CaCO₃ coatings are similar, which indicates that the corrosion resistance of these coatings at the early stage of embedment is similar. However, the impedance at the low frequency of both MAO and MAO/ DCPD coatings in Fig. 9(d) and (g) significantly decreased after being embedded for 96 h, which suggests that the MAO and MAO/ DCPD coatings gradually corroded in the PC paste with 3.5 wt %NaCl. On the contrary, the impedance at the low frequency of the MAO/ CaCO₃ coating increased after 96 h, which indicates that the corrosion resistance of the MAO/ CaCO₃ coating could increase during the embedment in the PC paste with 3.5 wt %NaCl.

Correspondingly, it can be clearly seen from the Nyquist plots in Fig. 9(c) that the diameter of the semi-circle for the MAO/ CaCO₃ coating at 1 h is only slightly larger than those of the MAO and MAO/ DCPD coatings, which implies that the CaCO₃ layer only slightly improves the corrosion resistance at the early stage of embedment. Nevertheless, the diameter of the semi-circle in the Nyquist plots for the MAO/ CaCO₃ coating becomes much larger than those of the MAO and MAO/ DCPD coatings during the prolonged embedment for 24 h and 96 h, which demonstrates that the long-term corrosion resistance of the MAO/ CaCO₃ coating is significantly higher than those of the MAO and MAO/ DCPD coatings.

Fig. 9(b, e, h) shows the Bode phase plots of the MAO, MAO/ DCPD and MAO/ CaCO₃ coatings during the prolonged embedment in the PC paste with 3.5 wt %NaCl. It can be seen that the Bode phase peak of MAO/ CaCO₃ coating at low frequency rises from 60° at the early stage to 80° after being embedded for 96 h. It is generally believed that the Bode phase peaks in the medium and low frequency range correspond to the electrochemical behaviors of oxide film and double layer, respectively. Thus, based on this, it can be deduced that the MAO/ CaCO₃ coating shows a self-healing property in the PC paste with 3.5 wt %NaCl. In contrast, the Bode phase peaks of the MAO and MAO/ DCPD coatings significantly decreased during the embedment period, which suggests that the MAO and MAO/ DCPD coatings were gradually damaged.

Here, three equivalent circuit models (Fig. 10) are proposed according to the previous research to further analyze the electrochemical properties and specific structural characteristics of the coating [37–39]. The constant phase element (CPE) using the Brug's formula [40] is used to denote the double layer capacitance (CPE_{dl}). Besides, the film capacitance (CPE_f) can be calculated by using the work of Hsu and

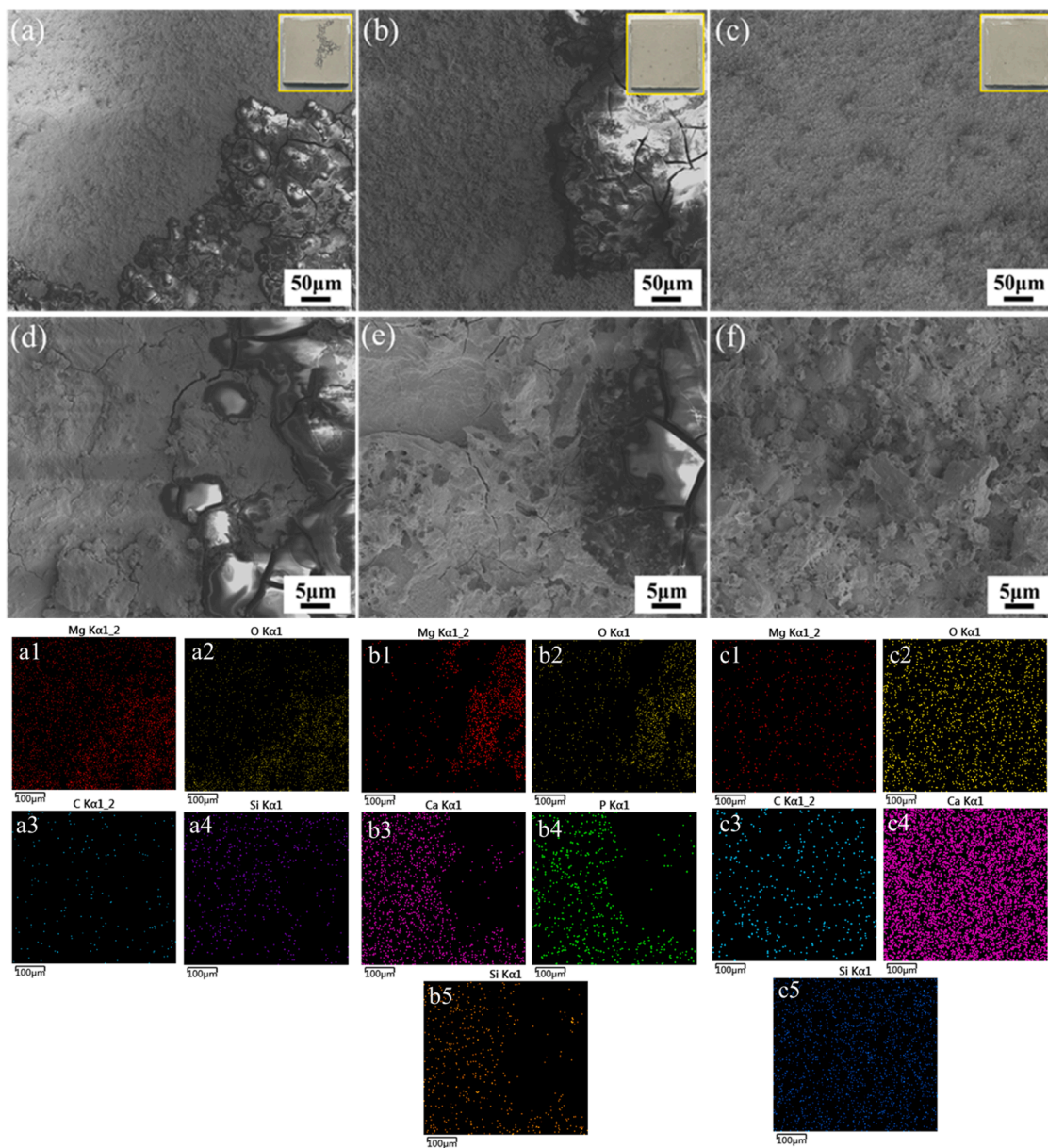


Fig. 7. : Surface morphologies of (a, d) MAO coating, (b, e) MAO/ DCPD coating and (c, f) MAO/ CaCO_3 coating after embedded in PC paste with 3.5 wt %NaCl for 96 h and the insets show the difference of the coatings. EDS analysis (a1)-(a4) corresponds to (a) MAO coating, (b1)-(b5) corresponds to (b) MAO/ DCPD coating and (c1)-(c5) corresponds to (c) MAO/ CaCO_3 coating.

Mansfeld [41] and Mark Orazem [42]. In addition, in these equivalent circuit models, R_s denotes the paste resistance, CPE_{dl} and R_{ct} represent double layer capacitance and charge transfer resistance, and CPE_f and R_f are assigned to the capacitance of oxide film and the total resistance of the pores on the coating, respectively. Besides, L and R_L are corresponding to inductance possibly associated with the relaxation process of adsorbed species and relevant inductance resistance. The fitting results are listed in Table 2.

As can be seen from the fitting data in Table 2, the R_f of MAO coating decreased from $5.19 \times 10^4 \Omega \cdot \text{cm}^2$ at 1 h to $2.50 \times 10^4 \Omega \cdot \text{cm}^2$ at 24 h and then keeps stable during the next 72 h ($2.72 \times 10^4 \Omega \cdot \text{cm}^2$). This indicates that the corrosion of the MAO coating mainly occurs during the first 24 h, which leads to the formation of corrosion products and in turn hinders the occurrence of the further corrosion. On the other hand, the R_f value of MAO/ DCPD coating has been decreasing during the whole embedment period, which is decreased from $5.40 \times 10^4 \Omega \cdot \text{cm}^2$ at 1 h to $2.05 \times 10^4 \Omega \cdot \text{cm}^2$ at 24 h and finally to a very low value of 5.54×10^3

$\Omega \cdot \text{cm}^2$ at 96 h. In contrast, the R_f value of the MAO/ CaCO_3 coating keeps relatively unchanged over the embedded time, which demonstrates that the MAO/ CaCO_3 coating is stable in the PC paste with 3.5 wt %NaCl. Correspondingly, the R_{ct} values of both MAO and MAO/ DCPD coatings decreased during the embedment period, which suggests that the exposure to PC paste with 3.5 wt %NaCl reduces the corrosion resistance of these coatings. Furthermore, it can be noted that the R_{ct} value of the MAO/ DCPD coating at 96 h is even lower than that of the MAO coating, which indicates that the DCPD layer even worsens the corrosion resistance of the coating. Similar observation has also been reported in the previous study [18] which could be attributed to coating at the bottom of large pore can be quite thin [43]. On the contrary, the R_{ct} value of the MAO/ CaCO_3 coating only slightly decreased during the first 1 h and then increased up to a R_{ct} value higher than the initial value ($1.34 \times 10^7 \Omega \cdot \text{cm}^2 \rightarrow 1.42 \times 10^7 \Omega \cdot \text{cm}^2$), thereby exhibiting a self-healing property. Moreover, the R_{ct} value of the MAO/ CaCO_3 coating at 96 h is more than two orders of magnitudes higher than those of the MAO and

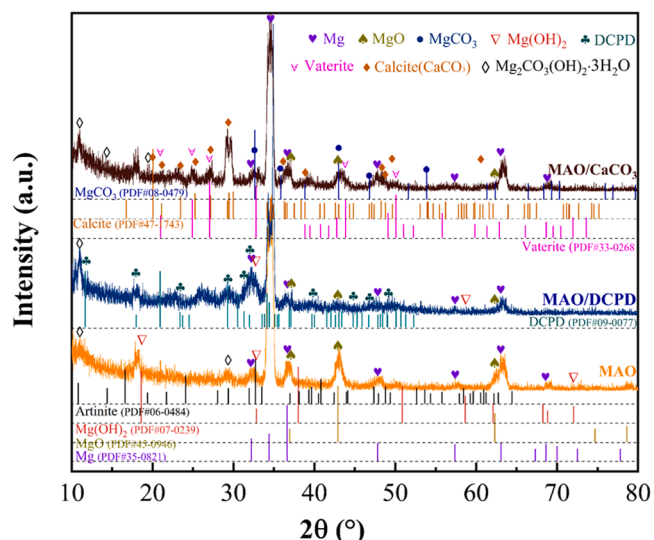


Fig. 8. : GIXRD patterns of MAO coating, MAO/DCPD coating and MAO/CaCO₃ coating after embedded in PC paste with 3.5 wt %NaCl for 96 h at an incident angle of 2°.

MAO/ DCPD coatings, which is indicative of a much better corrosion resistance of the MAO/ CaCO₃ coating in the PC paste with 3.5 wt % NaCl.

3.2.4. Surface morphology after immersion in the simulated concrete pore solutions

Because of the adhesion of PC pastes interferes with our vision, the surface morphologies of the MAO, MAO/DCPD and MAO/CaCO₃ coatings after corrosion were further obtained by the SEM characterization after immersion in the simulated concrete pore solutions with 3.5 wt % NaCl for 96 h, and the results are shown in Fig. 11. It can be observed in Fig. 11(a) that, cracks all over the surface of the MAO coating after immersion. This indicates that the Cl⁻ ions probably penetrate through the pores and results the corrosion of the substrate. Moreover, it is worthwhile noting that some enlarged pores appeared on the surface of the MAO coating after immersion, it is speculated that they possibly acted as the pathways for the corrosion agents during the period of immersion. Fig. 11(a1–a3) show the EDS results, it can be seen that the MAO coating after immersion mainly consists of Mg and O elements. Similarly, it can be seen from the surface morphology of the MAO/DCPD coating after corrosion that, cracks can also be observed on the surface and the intact DCPD particles also disappeared compared to the original morphology. This suggests that severe corrosion occurs on the MAO and MAO/DCPD coatings, which is consistent with the results embedded in the PC paste. The EDS results in Fig. 11(b1–b4) also demonstrate that Mg and O elements exist in the MAO/DCPD coating after immersion.

Similar result has also been reported in the previous literature, Gao et al. [44] deposited a layer of hydroxyapatite on the surface of the MAO coating, and cracks can be observed on the corrosion morphologies of the coating after immersion in the SBF. They explained this could be related to the dissolution of coating and oxidation of substrate. As a comparison, the surface morphology of the MAO/CaCO₃ coating

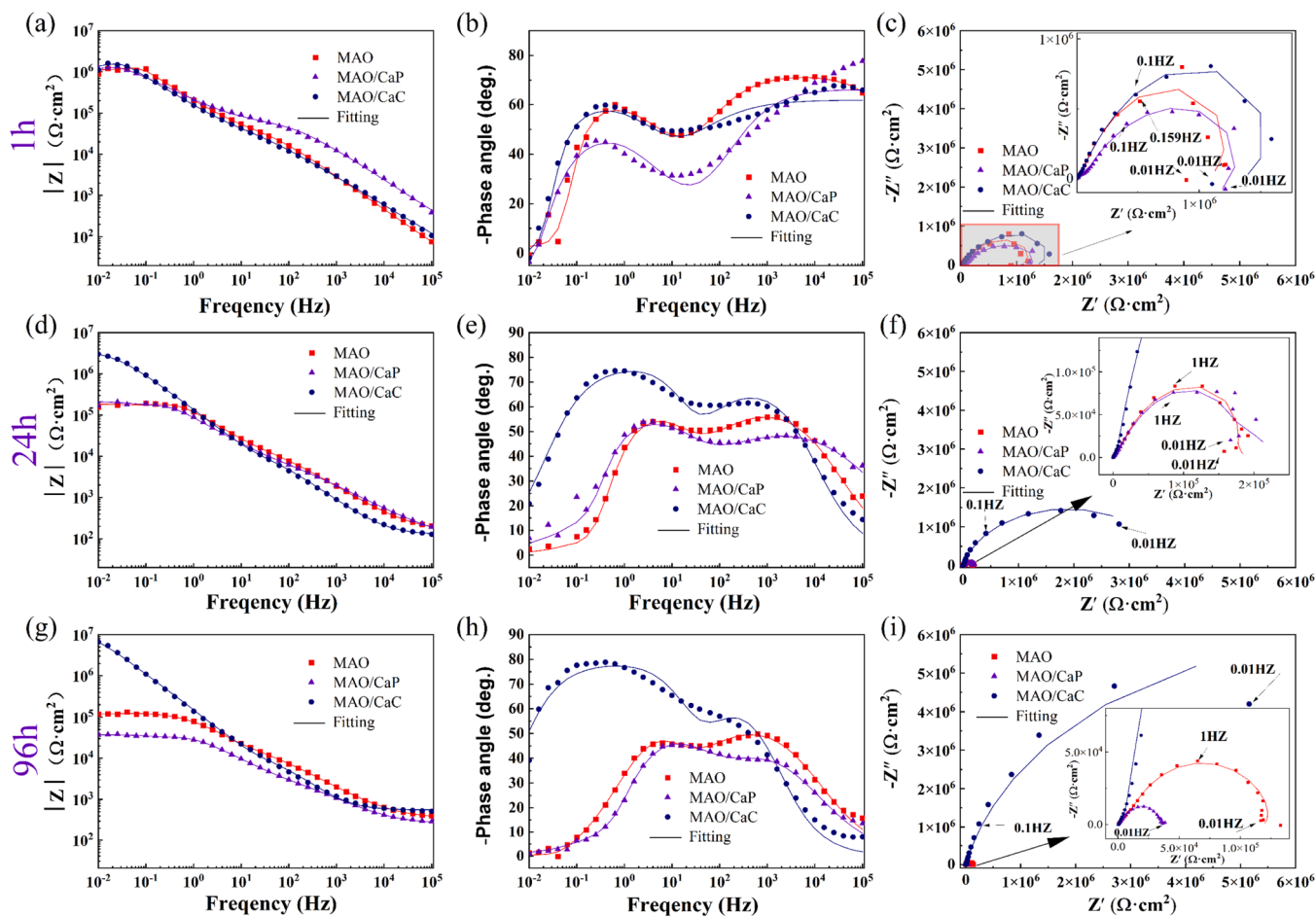


Fig. 9. : (a, d, g) Bode impedance plots, (b, e, h) Bode phase angle plots, and (c, f, i) Nyquist plots of all the investigated samples after embedded in PC paste with 3.5 wt %NaCl for (a–c) 1 h, (d–f) 24 h, (g–i) 96 h.

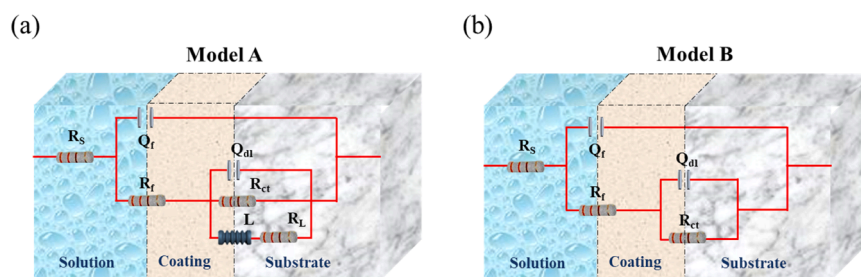


Fig. 10. : Equivalent electrical circuit models for EIS data fitting: (a) MAO coating, MAO/DCPD coating and MAO/CaCO₃ coating at 1 h, (b) MAO/CaCO₃ coating at 24 h and 96 h.

Table 2

Fitted EIS results for the different samples in PC paste based on the corresponding equivalent circuit models.

Time h	Alloys	R _s Ω·cm ²	Y _{0f} Ω ⁻¹ ·cm ⁻² ·s ⁿ	n _f	CPE _f	R _f Ω·cm ²	Y _{0dl} Ω ⁻¹ ·cm ⁻² ·s ⁿ	n _{dl}	CPE _{dl}	R _{ct} Ω·cm ²	R	L	Chi-Squared
1	MAO	10.14	2.90 × 10 ⁻⁷	0.81	0.52	5.19 × 10 ⁴	1.03 × 10 ⁻⁶	0.73	0.01	3.57 × 10 ⁶	1.67 × 10 ⁶	5.12 × 10 ⁶	5.98 × 10 ⁻³
	MAO/ CaP	8.06	8.69 × 10 ⁻⁸	0.77	0.75	5.87 × 10 ⁴	1.54 × 10 ⁻⁶	0.62	0.01	2.12 × 10 ⁶	1.51 × 10 ⁶	3.14 × 10 ⁷	8.97 × 10 ⁻³
	MAO/ CaC	10.00	8.41 × 10 ⁻⁷	0.69	0.29	6.81 × 10 ⁴	9.89 × 10 ⁻⁷	0.74	0.02	4.35 × 10 ⁶	1.90 × 10 ⁶	1.65 × 10 ⁷	8.35 × 10 ⁻³
24	MAO	154.9	1.11 × 10 ⁻⁶	0.71	0.15	2.50 × 10 ⁴	7.64 × 10 ⁻⁷	0.81	0.09	2.69 × 10 ⁵	4.07 × 10 ⁵	2.39 × 10 ⁵	2.60 × 10 ⁻³
	MAO/ CaP	79.84	2.72 × 10 ⁻⁶	0.60	0.04	2.05 × 10 ⁴	6.90 × 10 ⁻⁷	0.80	0.06	4.93 × 10 ⁵	3.66 × 10 ⁵	2.18 × 10 ⁵	4.77 × 10 ⁻³
	MAO/ CaC	125.5	1.17 × 10 ⁻⁶	0.80	0.12	2.95 × 10 ⁴	3.78 × 10 ⁻⁷	1.00	0.38	3.86 × 10 ⁶			4.89 × 10 ⁻³
96	MAO	344.0	1.58 × 10 ⁻⁶	0.67	0.14	2.72 × 10 ⁴	8.93 × 10 ⁻⁷	0.86	0.24	1.08 × 10 ⁵	6.95 × 10 ⁵	2.64 × 10 ⁶	1.31 × 10 ⁻³
	MAO/ CaP	247.8	4.21 × 10 ⁻⁶	0.62	0.17	5.54 × 10 ³	2.44 × 10 ⁻⁶	0.74	0.18	4.56 × 10 ⁴	1.11 × 10 ⁵	2.43 × 10 ⁴	7.51 × 10 ⁻⁴
	MAO/ CaC	572.1	1.06 × 10 ⁻⁶	0.82	0.14	7.57 × 10 ⁴	3.12 × 10 ⁻⁷	1.00	0.32	1.69 × 10 ⁷			1.78 × 10 ⁻²

presents a different feature. As shown in Fig. 11(c) and (f), it can be seen that a large area of cubic particles was attached on the surface of the original coating after immersion, the morphology of the particles is the same as the calcite in the MAO/CaCO₃ coating. This indicates that extra calcite generated during the immersion, which is consistent with the GIXRD results in Fig. 8. The EDS results in Fig. 11(c1-c4) also demonstrate that the MAO/CaCO₃ coating after immersion mainly consists of Ca, O and C elements. Therefore, the MAO/CaCO₃ coating exhibits a self-healing property, which is mainly ascribed the generation of extra calcite. The detailed discussion self-healing property will be mentioned in Section 3.3.2.

3.3. Discussion

3.3.1. Formation mechanism of the MAO/DCPD and MAO/CaCO₃ coatings

As introduced above, both DCPD and CaCO₃ coatings were fabricated on the as-prepared MAO coatings via ultrasound-assisted chemical conversion in this study. However, the corrosion behaviour of the MAO/DCPD and MAO/CaCO₃ coatings presented completely different features in the chloride-containing Portland cement system. This could be related to the different formation mechanisms of the DCPD and /CaCO₃ layer in the chemical solutions containing hydrogen phosphate or bicarbonate, respectively.

Many previous researches have already investigated the formation mechanism of the Ca/P coating prepared on the MAO coating [17,45]. Because of the existence of the as-prepared MAO coating, the dissolution of Mg is inhibited. However, the MgO in the MAO coating could still partly dissolve in the chemical solution with a pH of 4.06, as shown in Eq. (1).



It should be noted that, rather than PO₄³⁻ ions, the HPO₄²⁻ ions could be

dominant due to the pH of the preparation solutions [46]. Since the solubility product constant (K_{sp}) of Mg(OH)₂ (5.61×10^{-12}) is six orders lower than that of MgHPO₄ (1.67×10^{-6}), the dissolved Mg²⁺ ions preferentially combine with the OH⁻ ions rather than HPO₄²⁻ and thus the Mg(OH)₂ forms on the surface of MAO, which has been verified by the presence of the peaks of Mg(OH)₂ in the GIXRD patterns for the MAO/DCPD coating. Nevertheless, the intensity of Mg(OH)₂ in the GIXRD pattern for the MAO/DCPD coating is weak. This indicates that the layer of Mg(OH)₂ formed in the MAO/DCPD coating is thin, which could be attributed to the limited dissolution of MgO in the MAO layer [47]. This is different from the Ca/P coating directly fabricated on the Mg substrate. According to the previous research [48], compared to the Ca/P coating formed on MAO layer, the Ca/P coating fabricated on the Mg substrate usually possesses a much thick inner Mg(OH)₂ layer with a clear boundary with the Mg substrate. It is known that the Mg(OH)₂ layer formed on the Mg substrate could be ascribed to the dissolution of Mg alloy, as shown in Eq. (2) [49].



Consequently, the entrapment of hydrogen and even hydrogen atoms could result in the formation of penetrating cracks and thus the bonding between the outer Ca/P layer and the substrate could be affected [49]. Moreover, the further dissolution of Mg lead to the formation of a thicker Mg(OH)₂ layer. What's more, the assistance of ultrasonic applied in the coating preparation process can also help the formation of a denser coating via the removal of hydrogen bubbles [50]. In turn, the binding strength between the DCPD coating and the inner MgO layer was enhanced by the inhibition of Mg²⁺ ions as well as a dense layer. This can also be evident from the cross-sectional morphology of the MAO/DCPD coating that no obvious interface can be seen between the outer Ca/P layer and the inner MAO layer. In addition, the main formation process of the outer DCPD layer has been widely studied, which are shown in Eqs. (3 and 4) [47,51].

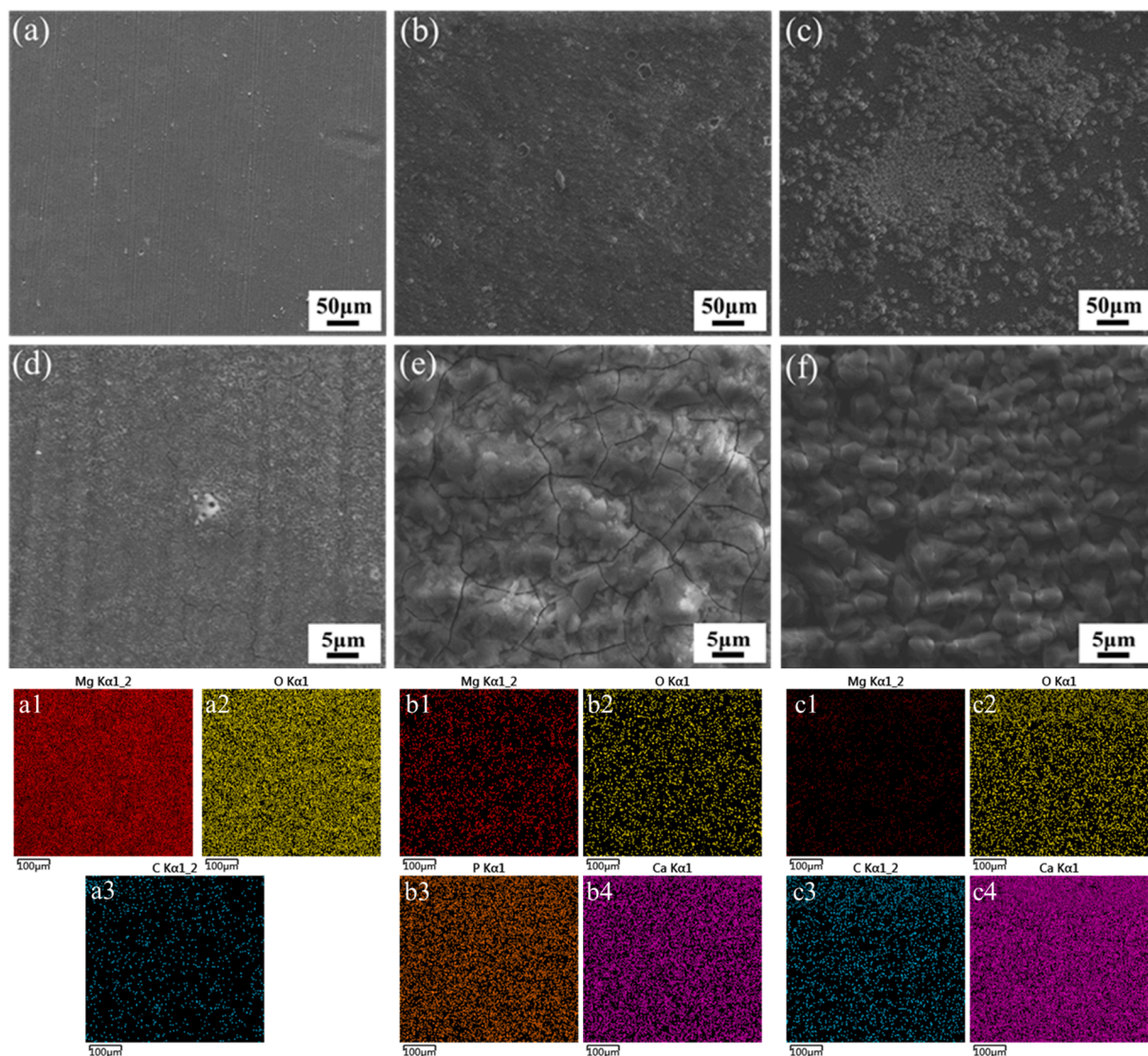
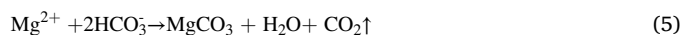


Fig. 11. : Surface morphologies of (a, d) MAO coating, (b, e) MAO/DCPD coating and (c, f) MAO/ CaCO₃ coating after immersion in the simulated concrete pore solutions with 3.5 wt % NaCl for 96 h. EDS analysis (a1)-(a3) corresponds to (a) MAO coating, (b1)-(b4) corresponds to (b) MAO/ DCPD coating and (c1)-(c4) corresponds to (c) MAO/ CaCO₃ coating.



Compared to the triple-layer structure of MAO/DCPD coating (DCPD + Mg(OH)₂ + MAO), the MAO/CaCO₃ coating exhibits a completely different structure (CaCO₃ + MgCO₃ + MAO). The electrochemical and chemical reactions occurred during the coating preparation process is probably as follows. Firstly, because of the barrier of the MgO layer, the dissolution of Mg from the Mg alloy is also inhibited in the chemical solution where CaCO₃ is precipitated. However, because of the acid environment in the chemical solution (pH=6.50), MgO could still dissolve in the solution, but may be fewer than that of the MAO/DCPD coating (pH=4.06), as shown in Eq. (1). Subsequently, the reaction could occur between the dissolved Mg²⁺ and HCO₃⁻ ions. It is worthwhile noting that although the solubility product constant (K_{sp}) of Mg(OH)₂ (5.61×10^{-12}) is much lower than that of MgCO₃ (6.82×10^{-8}), but the MgCO₃ is more stable with increasing HCO₃⁻ ions compared to Mg(OH)₂, previous research has already proved this [52]. Therefore, compared to Mg(OH)₂, MgCO₃ is favoured to precipitate in the solution

containing HCO₃⁻ ions. Moreover, because of the presence of saturated HCO₃⁻ and Ca²⁺ ions in the preparation solution, the nucleation of CaCO₃ will also occur in the solution. It should be noted that the nucleation energy barrier of calcium carbonate is much lower than magnesium carbonate [53], therefore, the nucleation of minerals formed on the near surface of the Mg alloy is a mixture of MgCO₃ and CaCO₃ with calcium being predominant, which can be defined as magnesian calcite ((Mg,Ca)CO₃) [54], as demonstrated in the GIXRD results. On the other hand, since the free Mg²⁺ is probably absent away from the MgO layer, HCO₃⁻ in the preparation solution could only react with Ca²⁺ and form CaCO₃ precipitates on top of MgO layer, which leads to the nucleation and growth of CaCO₃ in the outer layer of the coating. The corresponding reactions are shown in Eqs. (5 and 6) [20,55].



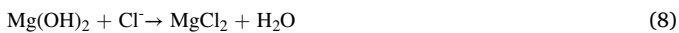
Therefore, different structures could be obtained in MAO/DCPD and MAO/CaCO₃ coatings due to the different chemical solutions applied in the coating preparation process. Although the ultrasound helps to accelerate the nucleation of both DCPD and CaCO₃ crystals, the DCPD

coating at the bottom of large pores can be thin [43] and voids can also be observed in the CaCO₃ coating. These could have a great impact on the corrosion resistance of the coatings. However, the biggest difference emphasized at the inner layer of MAO/DCPD and MAO/CaCO₃ coatings. The different Mg(OH)₂ and (Mg,Ca)CO₃ inner layers possibly influence the corrosion resistance of these coatings, which will be discussed in the next section.

3.3.2. Corrosion and self-healing mechanism of the coatings

According to the corrosion behaviour revealed by the EIS curves and the corroded morphologies, the MAO coating as well as the MAO/DCPD coating presented the decreased corrosion resistance during the embedment in the chloride-containing Portland cement system, while a self-healing performance can be obtained from the MAO/CaCO₃ coating.

When the MAO coated sample was firstly embedded in the PC paste or immersed in the simulated concrete solution, two main processes could take place: penetration of Cl⁻ towards the substrate through the coating defects including cracks and pores, and the dissolution of MgO [44]. Firstly, the Cl⁻ ions in the aggressive electrolyte could penetrate through the cracks and pores in the MAO coating, the enlarged white holes in Fig. 11(a) and (d) reveal the aggressive behaviour of chloride ions. In this process, the coating material MgO is converted to Mg(OH)₂ and then partly dissolved to soluble MgCl₂, the reactions are as the following [44,56]:



The corrosion mechanism of the MAO/DCPD coating may be a bit similar with the MAO coating, it mainly consists of the dissolution of the coating and the oxidation of substrate. However, the DCPD layer on the top of MgO layer provided extra protection than the MAO coating [45]. Therefore, the intrusion of chloride ions will be delayed, which can be evident from the surface of MAO/DCPD coating after embedment. However, the current density of the MAO/DCPD coating after embedded for 96 h (Fig. 6) dropped compared to the MAO coating, indicating no obvious increase in corrosion resistance. Previous research has also reported such results [18]. This may be due to the fact that both Mg(OH)₂ layer and DCPD layer generated by the above coating formation process mentioned are not dense enough and cannot resist the intrusion of Cl⁻ [43]. Once the corrosion pits are formed, the oxidation of the substrate and the dissolution of the coating material MgO as well as the DCPD layer would take place simultaneously, then the DCPD layer peeled off in the PC paste or in the simulated concrete solution. Moreover, it can be seen from Fig. 11(a) and (b) that, cracks covered the entire surface of MAO and MAO/DCPD coatings after corrosion. According to the previous research [57], it could be attributed by the dehydration of Mg(OH)₂ according to Eq. (9):



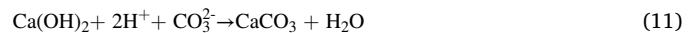
As the molar volume of Mg(OH)₂ is larger than that of MgO, therefore, when Mg(OH)₂ is dehydrated to MgO [44], the cracks are expected to be formed as observed in Fig. 11(a) and (b). The presence of cracks on the MAO/DCPD coating also indicates that the dissolution of the Ca/P layer after immersion for 96 h.

Compared to the other two kinds of coatings, the radius of the arc increased during the embedment and the EIS revolution of the MAO/CaCO₃ coating exhibits the typical feature of self-healing performance [58]. Therefore, the corrosion mechanism could be completely different from the other two coatings. It could also be speculated that the coating may have undergone some kinds of transformation or regrowth in the PC paste or simulated concrete pore solution.

Therefore, the corrosion protection mechanism for the MAO/CaCO₃ coating may be as follow. Firstly, like the DCPD layer on the top of the MgO layer, the CaCO₃ coating can also partly resist the penetration of

the aggressive ions. However, the aggressive electrolyte can still penetrate through the outer layer due to the existence of the voids between the CaCO₃ particles as shown in Fig. 2(c) and (f). Fortunately, the dense (Mg,Ca)CO₃ inner layer composed of CaCO₃ and MgCO₃ can provide extra protection [59], which shows better corrosion resistance than the inner Mg(OH)₂ layer in the MAO/DCPD coating.

At the same time, the self-healing performance of the outer CaCO₃ layer can be summarized based on the chemical reactions (10)-(13). Firstly, the presence of CO₂ and water in the PC paste or simulated concrete solution led to the formation of H⁺ and CO₃²⁻ as shown in Eq. (10). Then, according to the previous research [60], calcium hydroxide (Ca(OH)₂) could be formed in the Portland cement after hydration, then the calcium hydroxide will be transformed to the CaCO₃ with the reaction with H⁺ and CO₃²⁻ ions. Meanwhile, as can be seen in Fig. 11(c) and (f), the newly formed calcite is densely arranged, which may not be just a carbonization process as shown in Eq. (11). Therefore, it is deduced that although the crystallization of the CaCO₃ in the PC paste or in the simulated concrete solution occurs through the so-called dissolution-recrystallization mechanism, the deposition of regenerated CaCO₃ particles on the original MAO/CaCO₃ coating may through the solid-state transformation. In this process, the CaCO₃ particles in the original outer layer could directly react with the H⁺ and CO₃²⁻, which will cause the increase of active Ca²⁺ and HCO₃⁻ ions in the system (Eq. 12). Finally, the deposition reaction of the CaCO₃ crystals was promoted as shown in Eq. (13). The main chemical reactions are shown in Eqs. (10-13) [61-63], thereby exhibiting the self-healing performance.



According to the previous research, both calcite and vaterite can stable exist in the alkaline condition, which ensures the enough anti-corrosion performance of the MAO/CaCO₃ coating. The illustration of the corrosion protection mechanism of the three coatings is shown in Fig. 12.

4. Conclusions

In this study, for the promising enhanced corrosion resistance of the AZ41 alloy used for magnesium formwork, a microarc-oxidized coating was firstly fabricated on the surface of AZ41 Mg alloy. Afterwards, both DCPD and CaCO₃ coatings were used to seal the MAO coating. The materials characterization was used to analyze the morphology and composition of the coating. Moreover, the long-time electrochemical tests including EIS and potentiodynamic polarization were adopted to assess the corrosion resistance of the three as-prepared coatings in the chloride-containing Portland cement system up to 96 h. Based on the results obtained, the following conclusions can be drawn:

1. Both DCPD (CaHPO₄·H₂O) and CaCO₃ coatings were successfully prepared on the as-prepared MAO coating on the surface of AZ41 Mg alloy via ultrasound-assisted chemical conversion method for the promising enhancement on the corrosion resistance.
2. The MAO/DCPD coating consists of an outer DCPD layer and an inner Mg(OH)₂ layer, while the MAO/CaCO₃ coating is composed of an outer CaCO₃ layer and a dense (Mg,Ca)CO₃ inner layer.
3. The corrosion resistance of the MAO/CaCO₃ coating embedded in 3.5 %-NaCl PC paste is higher than those of both MAO coating and MAO/DCPD coating, with a corrosion current density of 3.229 × 10⁻⁷ A·cm⁻² even after 96 h.
4. The good anticorrosion of the MAO/CaCO₃ coating is benefitted by the triple-layer structure, which could be a result of the effect of

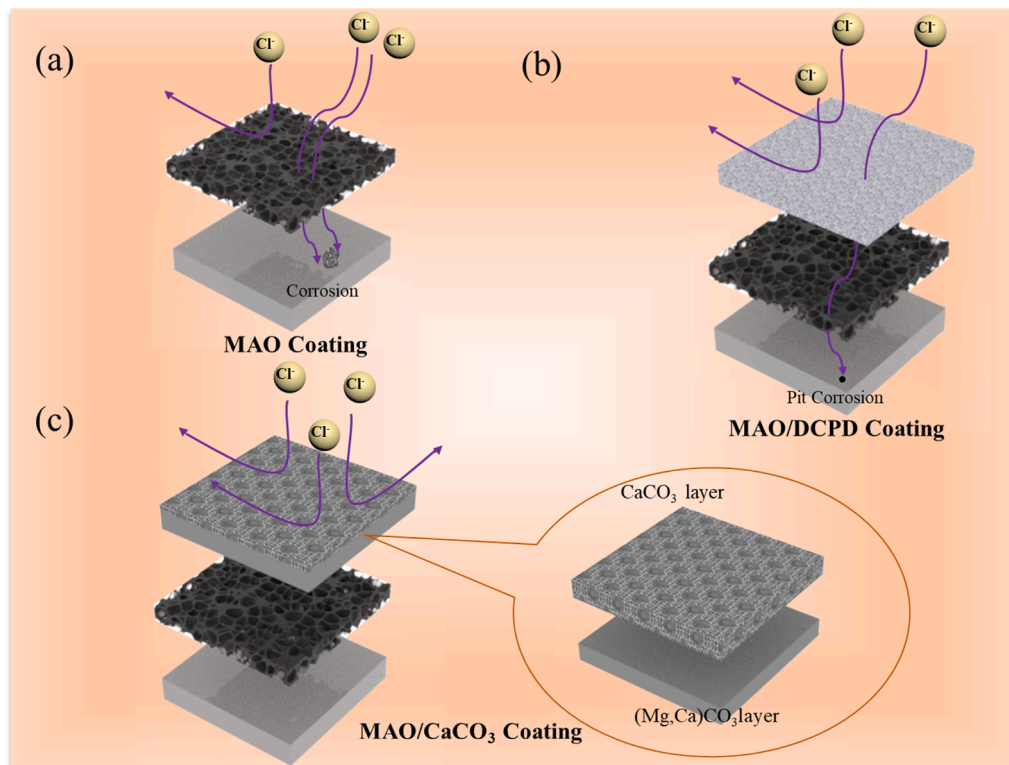


Fig. 12. : Corrosion protection mechanism of the (a) MAO coating, (b) MAO/DCPD coating and (c) MAO/CaCO₃ coating.

preparation solution chemistry and cavitation effect of ultrasound on the collapse process of the hydrogen bubble and the nucleation process of crystals.

5. The self-healing property of the MAO/CaCO₃ coating originated from the generation of extra CaCO₃(calcite), which can be attributed to the inspiration of concrete environment.

CRedit authorship contribution statement

Ye Wang: Conceptualization, Methodology, Investigation, Writing – original draft. **Di Yu:** Investigation, Writing – review & editing. **Kai Ma:** Data curation, Writing – review & editing. **Chaoneng Dai:** Data curation, Writing – review & editing. **Danqian Wang:** Supervision, Visualization, Writing – review & editing. **Jingfeng Wang:** Supervision, Conceptualization.

Declaration of Competing Interest

The authors declare that they have no known competing financial interests or personal relationships that could have appeared to influence the work reported in this paper.

Data availability

The raw/processed data required to reproduce these findings cannot be shared at this time as the data also forms part of an ongoing study.

Acknowledgements

The authors gratefully acknowledge the financial support from the National Key Research and Development Program of China (No. 2021YFB3701100), the Natural Science Foundation Commission of China (Grant No. U20A20234 and 51874062), Chongqing Foundation and Advanced Research Project (Grant No. cstc2019jcyj-zdxmX0010), the Science and Technology Major Project of Shanxi Province (No.

20191102008).

References

- [1] A.M. Brandt, Fibre reinforced cement-based (FRC) composites after over 40 years of development in building and civil engineering, *Compos. Struct.* 86 (2008) 3–9, <https://doi.org/10.1016/j.compstruct.2008.03.006>.
- [2] M.M. de Abreu, A.C. Lordsleem, Aluminum formwork system: loss and productivity, *Built Environ. Proj. Asset Manag.* 9 (2019) 616–627, <https://doi.org/10.1108/BEPAM-04-2018-0070>.
- [3] D. Wang, Y. Wang, J. Wang, K. Ma, C. Dai, J. Wang, F. Pan, Corrosion resistance of Mg-Al-Zn magnesium alloy concrete formwork in Portland cement paste, *Constr. Build. Mater.* 325 (2022), <https://doi.org/10.1016/j.conbuildmat.2022.126745>.
- [4] Y. Wang, G. Wu, C. Xu, Z. Yang, J. Sun, Revealing anti-corrosion behavior of magnesium alloy in simulated concrete pore solution, *Mater. Lett.* 285 (2021) 10–13, <https://doi.org/10.1016/j.matlet.2020.129047>.
- [5] G. Wu, J.M. Ibrahim, P.K. Chu, Surface design of biodegradable magnesium alloys - a review, *Surf. Coat. Technol.* 233 (2013) 2–12, <https://doi.org/10.1016/j.surfcoat.2012.10.009>.
- [6] L. Cai, X. Song, C.B. Liu, L.Y. Cui, S.Q. Li, F. Zhang, M. Bobby Kannan, D.C. Chen, R.C. Zeng, Corrosion resistance and mechanisms of Nd(NO₃)₃ and polyvinyl alcohol organic-inorganic hybrid material incorporated MAO coatings on AZ31 Mg alloy, *J. Colloid Interface Sci.* 630 (2023) 833–845, <https://doi.org/10.1016/j.jcis.2022.10.087>.
- [7] J. Chen, W. Lin, S. Liang, L. Zou, C. Wang, B. Wang, M. Yan, X. Cui, Effect of alloy cations on corrosion resistance of LDH/MAO coating on magnesium alloy, *Appl. Surf. Sci.* 463 (2019) 535–544, <https://doi.org/10.1016/j.apsusc.2018.08.242>.
- [8] X. Mei Wang, X. Li Fan, M. Qi Zeng, C. Yang Li, L. Yue Cui, X. Bo Chen, Y. Hong Zou, Z. Lin Wang, R. Chang Zeng, In vitro degradation resistance of glucose and L-cysteine-bioinspired Schiff-base anodic Ca-P coating on AZ31 magnesium alloy, *Trans. Nonferrous Met. Soc. China* 32 (2022) 1485–1500, [https://doi.org/10.1016/S1003-6326\(22\)65888-6](https://doi.org/10.1016/S1003-6326(22)65888-6).
- [9] K. Xue, P.H. Tan, Z.H. Zhao, L.Y. Cui, M.B. Kannan, S.Q. Li, C.B. Liu, Y.H. Zou, F. Zhang, Z.Y. Chen, R.C. Zeng, In vitro degradation and multi-antibacterial mechanisms of β-cyclodextrin@curcumin embodied Mg(OH)₂/MAO coating on AZ31 magnesium alloy, *J. Mater. Sci. Technol.* 132 (2023) 179–192, <https://doi.org/10.1016/j.jmst.2022.04.053>.
- [10] L. Cai, D. Mei, Z.Q. Zhang, Y. Ding Huang, L.Y. Cui, S.K. Guan, D.C. Chen, M. B. Kannan, Y. Feng Zheng, R.C. Zeng, Advances in bioorganic molecules inspired degradation and surface modifications on Mg and its alloys, *J. Magnes. Alloy* 10 (2022) 670–688, <https://doi.org/10.1016/j.jma.2022.02.005>.
- [11] A.M. Zhang, P. Lenin, R.C. Zeng, M.B. Kannan, Advances in hydroxyapatite coatings on biodegradable magnesium and its alloys, *J. Magnes. Alloy* 10 (2022) 1154–1170, <https://doi.org/10.1016/j.jma.2022.01.001>.

- [12] J.M. Wang, X. Sun, L. Song, M.B. Kannan, F. Zhang, L.Y. Cui, Y.H. Zou, S.Q. Li, R. C. Zeng, Corrosion resistance of Mg-Al-LDH steam coating on AZ80 Mg alloy: effects of citric acid pretreatment and intermetallic compounds, *J. Magnes. Alloy* (2022), <https://doi.org/10.1016/j.jma.2022.01.004>.
- [13] L. He, Y. Shao, S. Li, L. Cui, X. Ji, Y. Zhao, *Advances in layer-by-layer self-assembled coatings*, *Sci. China Mater.* 64 (2021) 2093–2106.
- [14] T.S.N.S. Narayanan. Conversion Coatings for Magnesium and its Alloys, 2022, <https://doi.org/10.1007/978-3-030-89976-9>.
- [15] T.S.N. Sankara Narayanan, I.S. Park, M.H. Lee, Strategies to improve the corrosion resistance of microarc oxidation (MAO) coated magnesium alloys for degradable implants: prospects and challenges, *Prog. Mater. Sci.* 60 (2014) 1–71, <https://doi.org/10.1016/j.pmatsci.2013.08.002>.
- [16] Z. Lin, T. Wang, X. Yu, X. Sun, H. Yang, Functionalization treatment of micro-arc oxidation coatings on magnesium alloys: a review, *J. Alloy. Compd.* 879 (2021), 160453, <https://doi.org/10.1016/j.jallcom.2021.160453>.
- [17] Y. Shi, M. Qi, Y. Chen, P. Shi, MAO-DCPD composite coating on Mg alloy for degradable implant applications, *Mater. Lett.* 65 (2011) 2201–2204, <https://doi.org/10.1016/j.matlet.2011.04.037>.
- [18] Y. Wu, Y. Wang, S. Tian, H. Li, Y. Zhao, D. Jia, Y. Zhou, Formation mechanism, degradation behavior, and cytocompatibility of a double-layered structural MAO/rGO-CaP coating on AZ31 Mg, *Colloids Surf. B Biointerfaces* 190 (2020), 110901, <https://doi.org/10.1016/j.colsurfb.2020.110901>.
- [19] S.Y. Kim, Y.K. Kim, M.H. Ryu, T.S. Bae, M.H. Lee, Corrosion resistance and bioactivity enhancement of MAO coated Mg alloy depending on the time of hydrothermal treatment in Ca-EDTA solution, *Sci. Rep.* 7 (2017), <https://doi.org/10.1038/s41598-017-08242-0>.
- [20] P. Jiang, R. Hou, S. Zhu, S. Guan, A robust calcium carbonate (CaCO₃) coating on biomedical MgZnCa alloy for promising corrosion protection, *Corros. Sci.* 198 (2022), <https://doi.org/10.1016/j.corsci.2022.110124>.
- [21] C.R. Blue, A. Giuffre, S. Mergelsberg, N. Han, J.J. De Yoreo, P.M. Dove, Chemical and physical controls on the transformation of amorphous calcium carbonate into crystalline CaCO₃ polymorphs, *Geochim. Cosmochim. Acta* 196 (2017) 179–196, <https://doi.org/10.1016/j.gca.2016.09.004>.
- [22] Y. Wang, G. Wu, Improving corrosion resistance of magnesium alloy in Cl⁻-containing simulated concrete pore solution by ultrasound-assisted chemical deposition, *Scanning* 2021 (2021), <https://doi.org/10.1155/2021/5462741>.
- [23] Y. Chen, L. Wu, W. Yao, Y. Chen, Z. Zhong, W. Ci, J. Wu, Z. Xie, Y. Yuan, F. Pan, A self-healing corrosion protection coating with graphene oxide carrying 8-hydroxyquinoline doped in layered double hydroxide on a micro-arc oxidation coating, *Corros. Sci.* 194 (2022), <https://doi.org/10.1016/j.corsci.2021.109941>.
- [24] Z. Eren, Ultrasound as a basic and auxiliary process for dye remediation: a review, *J. Environ. Manag.* 104 (2012) 127–141, <https://doi.org/10.1016/j.jenvman.2012.03.028>.
- [25] B.A. Taleatu, E. Omotoso, C. Lal, W.O. Makinde, K.T. Ogundele, E. Ajenifuja, A. R. Lasisi, M.A. Eleruja, G.T. Mola, XPS and some surface characterizations of electrodeposited MgO nanostructure, *Surf. Interface Anal.* 46 (2014) 372–377, <https://doi.org/10.1002/sia.5425>.
- [26] Y. Barbaux, M. Dekiouk, D. Le Maguer, L. Gengembre, D. Huchette, J. Grimblot, Bulk and surface analysis of a Fe-P-O oxydehydrogenation catalyst, *Appl. Catal. A, Gen.* 90 (1992) 51–60, [https://doi.org/10.1016/0926-860X\(92\)80247-A](https://doi.org/10.1016/0926-860X(92)80247-A).
- [27] D. Zhou, S. Wang, Y. Jia, X. Xiong, H. Yang, S. Liu, J. Tang, J. Zhang, D. Liu, L. Zheng, Y. Kuang, X. Sun, B. Liu, NiFe Hydroxide lattice tensile strain: enhancement of adsorption of oxygenated intermediates for efficient water oxidation catalysis, *Angew. Chem. - Int. Ed.* 58 (2019) 736–740, <https://doi.org/10.1002/anie.201809689>.
- [28] J. Baltrusaitis, C.R. Usher, V.H. Grassian, Reactions of sulfur dioxide on calcium carbonate single crystal and particle surfaces at the adsorbed water carbonate interface, *Phys. Chem. Chem. Phys.* 9 (2007) 3011–3024, <https://doi.org/10.1039/b617697f>.
- [29] V. Fournier, P. Marcus, I. Olefjord, Oxidation of magnesium, *Surf. Interface Anal.* 34 (2002) 494–497, <https://doi.org/10.1002/sia.1346>.
- [30] D. Ivnitski, K. Artyushkova, R.A. Rincón, P. Atanassov, H.R. Luckarift, G. R. Johnson, Entrapment of enzymes and carbon nanotubes in biologically synthesized silica: glucose oxidase-catalyzed direct electron transfer, *Small* 4 (2008) 357–364, <https://doi.org/10.1002/smll.200700725>.
- [31] C.S. Gopinath, S.G. Hegde, A.V. Ramaswamy, S. Mahapatra, Photoemission studies of polymorphic CaCO₃ materials, *Mater. Res. Bull.* 37 (2002) 1323–1332, [https://doi.org/10.1016/S0025-5408\(02\)00763-8](https://doi.org/10.1016/S0025-5408(02)00763-8).
- [32] R. Kumar, H.R. Inta, H.V.S.R.M. Koppiseti, S. Ganguli, S. Ghosh, V. Mahalingam, Electrochemical reconstruction of Zn_{0.3}Co_{2.7}(PO₄)₂·4H₂O for enhanced water oxidation performance, *ACS Appl. Energy Mater.* 3 (2020) 12088–12098, <https://doi.org/10.1021/acsaem.0c02200>.
- [33] G.Y. Liu, J. Hu, Z.K. Ding, C. Wang, Bioactive calcium phosphate coating formed on micro-arc oxidized magnesium by chemical deposition, *Appl. Surf. Sci.* 257 (2011) 2051–2057, <https://doi.org/10.1016/j.apsusc.2010.09.050>.
- [34] J. Luo, F. Kong, X. Ma, Role of Aspartic acid in the synthesis of spherical vaterite by the Ca(OH)₂-CO₂ reaction, *Cryst. Growth Des.* 16 (2016) 728–736, <https://doi.org/10.1021/acs.cgd.5b01333>.
- [35] C.Y. Li, X.L. Fan, R.C. Zeng, L.Y. Cui, S.Q. Li, F. Zhang, Q.K. He, M.B. Kannan, H. W. (George) Jiang, D.C. Chen, S.K. Guan, Corrosion resistance of in-situ growth of nano-sized Mg(OH)₂ on micro-arc oxidized magnesium alloy AZ31—Influence of EDTA, *J. Mater. Sci. Technol.* 35 (2019) 1088–1098, <https://doi.org/10.1016/j.jmst.2019.01.006>.
- [36] N.H. De Leeuw, S.C. Parker, Surface structure and morphology of calcium carbonate polymorphs calcite, aragonite, and vaterite: An atomistic approach, *J. Phys. Chem. B* 102 (1998) 2914–2922, <https://doi.org/10.1021/jp973210f>.
- [37] G. Duan, L. Yang, S. Liao, C. Zhang, X. Lu, Y. Yang, B. Zhang, Y. Wei, T. Zhang, B. Yu, X. Zhang, F. Wang, Designing for the chemical conversion coating with high corrosion resistance and low electrical contact resistance on AZ91D magnesium alloy, *Corros. Sci.* 135 (2018) 197–206, <https://doi.org/10.1016/j.corsci.2018.02.051>.
- [38] Q. Dong, J. Dai, K. Qian, H. Liu, X. Zhou, Q. Yao, M. Lu, C. Chu, F. Xue, J. Bai, Dual self-healing inorganic-organic hybrid coating on biomedical Mg, *Corros. Sci.* 200 (2022), 110230, <https://doi.org/10.1016/j.corsci.2022.110230>.
- [39] M. Jamesh, S. Kumar, T.S.N. Sankara Narayanan, Corrosion behavior of commercially pure Mg and ZM21 Mg alloy in Ringer's solution - long term evaluation by EIS, *Corros. Sci.* 53 (2011) 645–654, <https://doi.org/10.1016/j.corsci.2010.10.011>.
- [40] G.J. Brug, A.L.G. van den Eeden, M. Sluyters-Rehbach, J.H. Sluyters, The analysis of electrode impedances complicated by the presence of a constant phase element, *J. Electroanal. Chem.* 176 (1984) 275–295, [https://doi.org/10.1016/S0022-0728\(84\)80324-1](https://doi.org/10.1016/S0022-0728(84)80324-1).
- [41] C.H. Hsu, F. Mansfeld, Technical note: concerning the conversion of the constant phase element parameter Y₀ into a capacitance, *Corrosion* 57 (2001) 747–748, <https://doi.org/10.5006/1.3280607>.
- [42] B. Hirschorn, M.E. Orazem, B. Tribollet, V. Vivier, I. Frateur, M. Musiani, Determination of effective capacitance and film thickness from constant-phase-element parameters, *Electrochim. Acta* 55 (2010) 6218–6227, <https://doi.org/10.1016/j.electacta.2009.10.065>.
- [43] L. Chang, L. Tian, W. Liu, X. Duan, Formation of dicalcium phosphate dihydrate on magnesium alloy by micro-arc oxidation coupled with hydrothermal treatment, *Corros. Sci.* 72 (2013) 118–124, <https://doi.org/10.1016/j.corsci.2013.03.017>.
- [44] Y. Gao, A. Yerokhin, A. Matthews, Deposition and evaluation of duplex hydroxyapatite and plasma electrolytic oxidation coatings on magnesium, *Surf. Coat. Technol.* 269 (2015) 170–182, <https://doi.org/10.1016/j.surfcoat.2015.01.030>.
- [45] G.Y. Liu, J. Hu, Z.K. Ding, C. Wang, Formation mechanism of calcium phosphate coating on micro-arc oxidized magnesium, *Mater. Chem. Phys.* 130 (2011) 1118–1124, <https://doi.org/10.1016/j.matchemphys.2011.08.043>.
- [46] O. Rybalkina, K. Tsygurina, E. Melnikova, S. Mareev, I. Moroz, V. Nikonenko, N. Pismenskaya, Partial fluxes of phosphoric acid anions through anion-exchange membranes in the course of NaH₂PO₄ solution electro dialysis, *Int. J. Mol. Sci.* 20 (2019), <https://doi.org/10.3390/ijms20143593>.
- [47] J. Han, S. Tang, H. San, X. Sun, J. Hu, Y. Yu, Formation mechanism of calcium phosphate coating on a plasma electrolytic oxidized magnesium and its corrosion behavior in simulated body fluids, *J. Alloy. Compd.* 818 (2020), 152834, <https://doi.org/10.1016/j.jallcom.2019.152834>.
- [48] Y. Wang, G. Wu, Improving corrosion resistance of magnesium alloy in Cl⁻-containing simulated concrete pore solution by ultrasound-assisted chemical deposition, *Scanning* 2021 (2021) 1–12, <https://doi.org/10.1155/2021/5462741>.
- [49] P. Zhou, B. Yu, Y. Hou, G. Duan, L. Yang, B. Zhang, T. Zhang, F. Wang, Revisiting the cracking of chemical conversion coating on magnesium alloys, *Corros. Sci.* 178 (2021), <https://doi.org/10.1016/j.corsci.2020.109069>.
- [50] J.M. Costa, A.F. de Almeida Neto, Ultrasound-assisted electrodeposition and synthesis of alloys and composite materials: a review, *Ultrason. Sonochem.* 68 (2020), 105193, <https://doi.org/10.1016/j.ultsonch.2020.105193>.
- [51] L.Y. Li, L.Y. Cui, L. Bin, R.C. Zeng, X.B. Chen, S.Q. Li, Z.L. Wang, E.H. Han, Corrosion resistance of glucose-induced hydrothermal calcium phosphate coating on pure magnesium, *Appl. Surf. Sci.* 465 (2019) 1066–1077, <https://doi.org/10.1016/j.apsusc.2018.09.203>.
- [52] L. Wang, T. Shinohara, B.P. Zhang, Influence of chloride, sulfate and bicarbonate anions on the corrosion behavior of AZ31 magnesium alloy, *J. Alloy. Compd.* 496 (2010) 500–507, <https://doi.org/10.1016/j.jallcom.2010.02.088>.
- [53] D. Toroz, F. Song, G.A. Chass, D. Di Tommaso, New insights into the role of solution additive anions in Mg²⁺-dehydration: implications for mineral carbonation, *CrystEngComm* 23 (2021) 4896–4900, <https://doi.org/10.1039/d1ce00052g>.
- [54] L.N. Lammers, E.H. Mitnick, Magnesian calcite solid solution thermodynamics inferred from authigenic deep-sea carbonate, *Geochim. Cosmochim. Acta* 248 (2019) 343–355, <https://doi.org/10.1016/j.gca.2019.01.006>.
- [55] R.C. Zeng, Y. Hu, S.K. Guan, H.Z. Cui, E.H. Han, Corrosion of magnesium alloy AZ31: the influence of bicarbonate, sulphate, hydrogen phosphate and dihydrogen phosphate ions in saline solution, *Corros. Sci.* 86 (2014) 171–182, <https://doi.org/10.1016/j.corsci.2014.05.006>.
- [56] M. Pannach, S. Bette, D. Freyer, Solubility equilibria in the system Mg(OH)₂-MgCl₂-H₂O from 298 to 393 K, *J. Chem. Eng. Data.* 62 (2017) 1384–1396, <https://doi.org/10.1021/acs.jced.6b00928>.
- [57] A.A. Aal, Protective coating for magnesium alloy, *J. Mater. Sci.* 43 (2008) 2947–2954, <https://doi.org/10.1007/s10853-007-1796-2>.
- [58] H. Chen, Z. Wu, Z. Su, S. Chen, C. Yan, M. Al-Mamun, Y. Tang, S. Zhang, A mechanically robust self-healing binder for silicon anode in lithium ion batteries, *Nano Energy* 81 (2021), 105654, <https://doi.org/10.1016/j.nanoen.2020.105654>.
- [59] D.B. Prabhu, P. Gopalakrishnan, K.R. Ravi, Morphological studies on the development of chemical conversion coating on surface of Mg–4Zn alloy and its corrosion and bio mineralisation behaviour in simulated body fluid, *J. Alloy. Compd.* 812 (2020), 152146, <https://doi.org/10.1016/j.jallcom.2019.152146>.
- [60] T. Yoshioka, I. Sawai, Studies on the hydration of portland cement, *J. Soc. Chem. Ind. Jpn.* 28 (1925) 32–41, <https://doi.org/10.1246/nikkashi1898.28.32>.

- [61] B.G. Kutchko, B.R. Strazisar, D.A. Dzombak, G.V. Lowry, N. Thauiov, Degradation of well cement by CO₂ under geologic sequestration conditions, *Environ. Sci. Technol.* 41 (2007) 4787–4792, <https://doi.org/10.1021/es062828c>.
- [62] M. Bagheri, S.M. Shariatipour, E. Ganjian, A review of oil well cement alteration in CO₂-rich environments, *Constr. Build. Mater.* 186 (2018) 946–968, <https://doi.org/10.1016/j.conbuildmat.2018.07.250>.
- [63] G. dos S. Batista, L.B. Schemmer, T. de A. Siqueira, E.M. da Costa, Chemical resistance and mechanical properties of nanosilica addition in oil well cement, *J. Pet. Sci. Eng.* 196 (2021), 107742, <https://doi.org/10.1016/j.petrol.2020.107742>.